Journal of Wind Engineering & Industrial Aerodynamics 257 (2025) 105993

Contents lists available at ScienceDirect

Journal of Wind Engineering & Industrial Aerodynamics

journal homepage: www.elsevier.com/locate/jweia

Square-section prism with rounded edges in a uniform cross-flow: Effect of incidence angle and Reynolds number on the (un)steady aerodynamics and proneness to galloping

Nils Paul van Hinsberg *, Annika Frede [1]

Institute of Aerodynamics and Flow Technology, German Aerospace Center, Göttingen, Germany

ARTICLE INFO

Keywords:
Reynolds number
Incidence angle
Flow separation
Rounded edges
Square section prism
Bluff body
Surface roughness
Wind tunnel
Galloping

ABSTRACT

The steady and unsteady aerodynamics of a slightly rough square-section prism with rounded edges of $r/D = 0.16$ is studied experimentally for a wide range of Reynolds numbers and incidence angles. Surface pressures, time-averaged and fluctuating lift, drag, and pitch moment coefficients, as well as eddy shedding frequencies are measured simultaneously for Reynolds numbers between 100,000 and 8 million. Analysis of the data reveals drastic changes in the cross-sectional surface pressure distribution with increasing Reynolds number for all incidence angles between −45° and 3.25°, caused by the promotion of the separated-shear-layer reattachment on the side faces owing to the rounded edges. At $\alpha = 0°$, an unbounded supercritical flow regime exists, while at larger absolute incidence angles the upper transition and transcritical flow regimes appear and gradually spread over an increasing range of Reynolds numbers. The transitions from the critical to the supercritical flow regime and further to the upper transition are accompanied by sign reversals of the lift and pitch moment. Thereupon, the classical quasi-steady galloping models are applied to determine the stability boundaries of transverse and torsional galloping depending on the incidence angle and Reynolds number. Moreover, at specific combinations of both governing parameters the eddy shedding is fully suppressed.

1. Introduction

Investigations on flow phenomena around rigid prismatic bluff bodies with square cross-sections and longitudinal sharp edges have received considerable attention, motivated by applications in many different fields related to civil and mechanical engineering, as well as in marine sciences and on- and offshore wind engineering. The flow over such prisms is characterised by many complex phenomena that all occur simultaneously, such as boundary-layer transition and separation, shear-layer instability and reattachment, regular and irregular eddy formation and shedding, and a strong three-dimensional wake flow.

For Reynolds numbers beyond 10^4, two-dimensional, i.e. "infinite", square-section prisms – positioned at 0° angle of incidence in a steady and uniform cross-flow – possess a constant high drag coefficient of $C_D = 2.15$–2.2, constant lift and drag fluctuations of about 1.0 and 0.1–0.15, respectively, and Strouhal numbers of 0.11 to 0.13 (Bai and Alam, 2018; van Hinsberg, 2021b). The Reynolds number Re_D is hereby defined as

$$Re_D = \frac{\rho U_\infty D}{\mu} \tag{1}$$

where ρ equals the density of the fluid, U_∞ the free stream velocity, D the width of each face of the prism, and μ the dynamic viscosity of the fluid. The independency of their fluid dynamics on the Reynolds number as governing parameter results from the fixed location of the boundary-layer separation at the sharp leading edges of the prism, as has been demonstrated by many experimental and numerical studies, e.g. Delany and Sorensen (1953), Vickery (1966), Bearman (1972), Lee (1975), Okajima (1982), Norberg (1993), Luo et al. (1994), Lyn et al. (1995), Tamura and Miyagi (1999), van Oudheusden et al. (2005, 2007), Huang et al. (2010), Huang and Lin (2011), Carassale et al. (2014), Bai and Alam (2018), van Hinsberg (2021b).

In contrast, both the flow topology and the resultant aerodynamic loading show a significant dependency on the angle of incidence. With increasing incidence angle from $\alpha = 0°$ to 45°, three different "angle-based" flow regimes are passed one after another (Igarashi, 1984): the *perfect separated* flow regime for $\alpha \leq \alpha_{cr} = 12°$–$15°$, the *reattachment* or *separation* flow regime ($\alpha = 12°$–$15°$ up to 35°), and the *wedge* or *attached* flow regime for $\alpha > 35°$. The boundary between the first two flow regimes is marked by the critical incidence angle α_{cr}, at which

* Corresponding author.
E-mail address: nils.vanhinsberg@dlr.de (N.P. van Hinsberg).
[1] Present: Institute of Fluid Mechanics, Karlsruhe Institute of Technology, Karlsruhe, Germany

https://doi.org/10.1016/j.jweia.2024.105993
Received 25 March 2024; Received in revised form 25 November 2024; Accepted 5 December 2024
Available online 17 December 2024

both the base pressure and the drag reach their minimum values, while the time-averaged lift and Strouhal number obtain their highest values (e.g. Lee (1975), Rockwell (1977), Obasaju (1983), Knisely (1990), Chen and Liu (1999), Dutta et al. (2003), van Oudheusden et al. (2005, 2007), Huang et al. (2010), Huang and Lin (2011), Yen and Yang (2011), Carassale et al. (2014)). These phenomena are related to the reattachment of the free shear layer on the downstream portion of the face that has been turned into the flow at $\alpha_{cr} \leq \alpha \leq 35°$. A separation bubble is formed on that side face of the square-section prism, which gradually decreases in size with increasing incidence angle within the separation flow regime and has disappeared completely once the *wedge* flow regime is entered (Huang et al., 2010; Huang and Lin, 2011). Depending on its exact value in combination with the Reynolds number, the incidence angle behaves either as a pure influencing parameter, as an additional governing parameter besides the Reynolds number, or as the sole governing parameter in the case the Reynolds number exceeds $\mathcal{O}(10^4)$.

1.1. Flow-induced vibrations: transverse and rotational galloping

When mounted elastically to allow a degree of freedom in rotation round the longitudinal axis and/or a translation in flow and cross-flow direction, a rigid square-section prism can undergo flow-induced vibrations in a uniform, oscillating, or unsteady incoming flow (Naudascher and Rockwell, 1994; Moe and Henriksen, 1999; Blevins, 2006; Païdoussis et al., 2011). The development of a (harmonically) changing pressure distribution over the cross-sectional surface of the prism, induced either by the (periodic) shedding of eddies in its wake or by the motion of the prism itself, leads to alternatingly fluctuating fluid-dynamic loads both in flow and in cross-flow direction, as well as in time-dependent torsional moments. Their magnitudes can reach such considerable values that the prism may experience one of the different types of flow-induced excitations, like vortex-induced vibrations (*VIV*) both in flow and cross-flow direction and motion-induced vibrations such as *one-degree-of-freedom plunge (i.e. transverse) or torsional galloping*.

VIV is an instability-induced excitation that comprises oscillations with high frequencies and limited amplitudes within a small range of reduced flow velocities. Galloping, on the other hand, is a self-excited limit cycle oscillation (LCO) that arises from the motion of the vibrating prism itself. Depending on the value of the reduced flow velocity and the cross-sectional dimensions of the prism, a distinction can be made between *low-speed* and *high-speed galloping*. In the case of transverse galloping, the low-speed variant is – based on the value of the total damping – situated below or at the lower boundary of vortex-shedding lock-in, i.e. for reduced velocities $U^\star = U_\infty/(f_y h) \leq U^\star_{VIV}$, where f_y equals the frequency of the transverse motion and h the height of the prism's cross-section perpendicular to the oncoming undisturbed flow. Low-speed galloping is related to the waviness of the separated shear layers and their flapping motion, as well as to the possible appearance of motion-induced eddies in the near wake behind the prism (Païdoussis et al., 2011). Moreover and similar to VIV, this galloping variant not only occurs within a limited range of reduced flow velocities, but the obtained maximum oscillation amplitudes of the resultant LCO is bounded as well. Nakamura and Matsukawa (1987) and Nakamura and Hirata (1989, 1991, 1994) showed that for prisms with sharp-edged rectangular cross-sections only those having cross-sectional shapes below the critical value of $(d/h)_{cr} \approx 0.6$ (hence, "short" to "shallow" prisms whereby d equals the length of the prism's cross-section in flow direction) are prone to low-speed galloping. High-speed galloping, then again, takes place at $U^\star \geq U^\star_{VIV}$, its exact value once again depending on the overall damping. It is furthermore marked by an oscillation amplitude that grows with increasing reduced velocity. In the current study, we have focused only on the high-speed transverse and torsional galloping variants.

For galloping to occur, the prism has to experience at its initial rest position small oscillations in translational or torsional direction around its static equilibrium position, induced by the fluctuating lift and drag forces or pitch moment, respectively. Since in this rest position the free shear layers do not reattach to any of the faces of the prism, the resultant of the lift and drag force or the torsional moment can act in the same direction of the translational or angular velocity. This leads to a dynamically instable situation, as the periodic motion itself induces a negative dynamic damping, i.e. the fluctuating fluid force or torsional moment tends to increase the motion of the prism (Parkinson, 1989; Nakamura and Hirata, 1994; Luo et al., 2003). The vibration amplitude thus steadily increases over each vibration cycle. At a fixed reduced velocity above the onset velocity of galloping, the maximum possible vibration amplitude is self-limited though, which results in the appearance of the LCO. This self-limitation of the amplitude is evoked by the alternating reattachment of both free shear layers to the side faces around the critical angle of incidence. Dependent on the combination of reduced velocity, Reynolds number, and the turbulence intensity of the oncoming flow, the transverse or angular vibration amplitude of square-section prisms can reach very large values. It is therefore not surprising that galloping ends not seldom in a failure of vibrating parts or a total collapse of a structure (Gupta et al., 1994; Valentín et al., 2022).

For the modelling of both transverse and rotational galloping oscillations, a linearised quasi-steady fluid-dynamic approach is commonly adopted. For this theory to be applicable to both galloping modes, the frequencies of the limit cycle oscillations must lie below certain values with respect to the frequencies of the natural eddy shedding. Otherwise, disturbances that have been introduced into the flow by the motion of the prism at a certain phase of the oscillation, i.e. at a specific incidence angle of the body to the oncoming flow, have not been carried far enough downstream with the flow in the wake behind the prism. In those cases, they are therefore still able to directly influence the flow around the prism at exactly the same vibration phase one oscillation period later. Provided that the eddy shedding and the vibration of the prism are not mutually influenced, a prediction of the galloping response can be made by using the characteristics of the mean, i.e. time-averaged fluid-dynamic force and the pitch moment obtained under static conditions at the appropriate effective incidence angle for transverse and rotational galloping, respectively (Slater, 1969; Nakamura and Mizota, 1975; Parkinson, 1989). However, it should be emphasised that the quasi-steady theory can only be used to obtain a preliminary verification of the possible proneness of the prism to galloping in quite a fast way with relatively little effort. For a more precise and reliable confirmation, the non-linear fluid-dynamic theory has to be used, since the latter also takes into account the unsteady effects that appear as a result of a phase lag between the motion of the prism and the surrounding viscous flow (Nakamura and Mizota, 1975; Nakamura, 1979).

1.2. Lateral edge rounding of two-dimensional square-section prisms

Two-dimensional sharp-edged square-section prisms experience not only a large mean drag and strong fluctuations of the transverse component of the overall fluid-dynamic force, but they are in addition also highly prone to the self-excited transverse galloping motion. A rounding of their sharp lateral edges is nowadays a well-established countermeasure to significantly reduce all three negative fluid-dynamic properties. The edge roundness provokes a more complex boundary layer behaviour over the surface of the prism, as it allows for a meandering of the transition points, the boundary-layer separation locations, and the free-shear-layer reattachment positions along the partially rounded cross-section in up- and downstream direction with both varying incidence angle and Reynolds number. Hence, a dependency on the Reynolds number of both the fluid dynamics of the

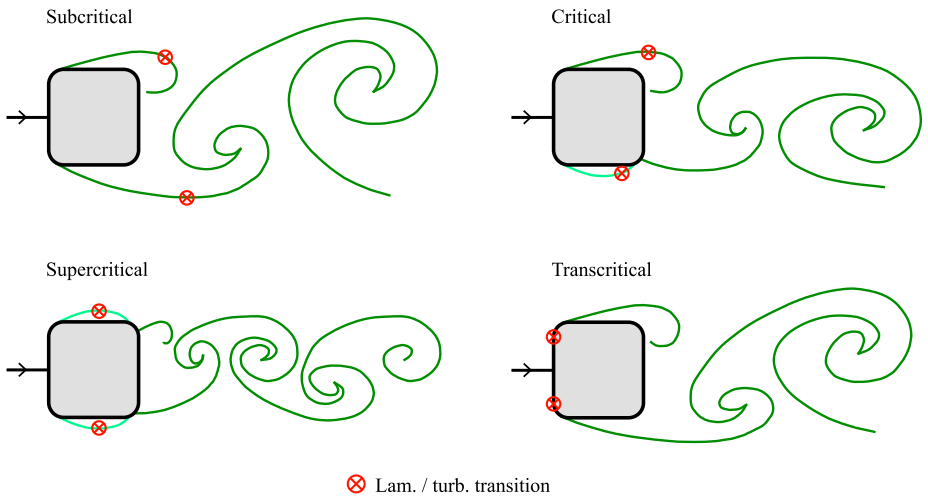

Fig. 1. Simplified sketches of the instantaneous two-dimensional flow fields that are typical for the individual Reynolds-number flow regimes around a static two-dimensional square-section prism with rounded edges positioned at $\alpha = 0°$ in a steady and uniform cross-flow. The key role is played by the location of the laminar-to-turbulent transition that gradually wanders upstream with increasing Reynolds number.

prism and the flow structures in its wake is thereby re-introduced for Reynolds numbers above 10^4.

Similar to circular cylinder flows, the trends of the aerodynamic coefficients as function of increasing Reynolds number of two-dimensional rounded square-section prisms in a steady and uniform cross-flow can generally be split up into four regimes, namely subcritical, critical, supercritical (including the upper transition), and transcritical (e.g. van Hinsberg et al. (2017, 2018), van Hinsberg (2021b)). In the first of these four regimes, the boundary layer remains laminar along the surface of the prism up to separation and the transition to turbulence takes place on both free shear layers in the near wake, as shown in the upper left image of Fig. 1. The two free shear layers remain separated from the prism's surface before rolling up into distinct vortices in the base region, which leads to a constant high drag coefficient and low Strouhal number, i.e. a low shedding frequency of the eddies. At subcritical Reynolds numbers, both aerodynamic parameters depend only very weakly on the Reynolds number. The following critical Reynolds-number flow regime is mainly characterised by a gradual, continuous upstream motion of the laminar/turbulent transition location along each of the two free shear layers with increasing Reynolds number. This upstream shift in transition induces a reduction of their lateral spread, owing to which each free shear layer gradually approaches a side face of the prism. Consequently, a moderate to strong decrease and increase of, respectively, the mean drag coefficient (i.e. the appearance of the characteristic "drag crisis") and the Strouhal number can be observed. Once the transition location is situated above a prism's side face, shear layer reattachment can occur, thereby forming a separation bubble on this side face (upper right image in Fig. 1). The attached turbulent boundary layer separates over the downstream-directed rounded edge and induces in this way not only a further decrease of the suction force at the base face of the prism, but also a smaller wake width. The combination of both occurrences results in an even stronger reduction of the mean drag force and a significant increase of the Strouhal number. Because the shear-layer reattachment does generally not occur at both side faces at exact equal Reynolds number, there exists a small Reynolds-number range within the critical flow regime that is characterised by a one-sided separation bubble, the "asymmetric (bistable) flow state". It is defined by a steady mean lift force on and a clear three-dimensionality of the flow around the prism, as well as by a hysteresis in the flow phenomena between increasing and decreasing Reynolds numbers (van Hinsberg et al., 2017). At the end of this regime, the critical Reynolds number with the lowest mean drag force and the highest Strouhal number is reached, which marks the transition of the critical to the supercritical flow regime. This latter regime is defined by a symmetric flow field around the prism due to the presence of a separation bubble on each of the two side faces of the prism, as shown in the lower left image of Fig. 1. It leads to a low and relatively constant value of the mean drag coefficient and a high Strouhal number. The passage from the supercritical to the transcritical Reynolds-number regime occurs over the upper transition and is accompanied by a widening of the wake that leads not only to a decrease of the mean base pressure and thus an increase in the mean drag coefficient, but also to a reduction of the Strouhal number. All of these changes result from the steady shrinkage of the two separation bubbles, their subsequent unsteady bursting and gradual disappearance. This highly unsteady behaviour of the separation bubbles is caused by the continuation of the upstream wandering of the transition location along the outer surface of the separation bubbles and its subsequent overtaking of the boundary-layer separation location for larger Reynolds numbers within the upper transition. In the last Reynolds-number flow regime, i.e. the transcritical regime, the transition to turbulence occurs is positioned at a fixed location – most probably in the vicinity of the stagnation point – and thus well upstream of the boundary layer separation locations, as shown in the lower right image of Fig. 1. The flow around the prism and in its wake is to a very large extend independent of the Reynolds number, which therefore also counts for the values of the mean base pressure, the mean and fluctuating aerodynamic force coefficients, and the Strouhal number.

The separated and combined effect of edge roundness and angle of incidence on the fluid-dynamic loading, the flow topology, and on the heat transfer of square-section prisms has been subject of extensive research for Reynolds numbers up to $\mathcal{O}(10^3)$, see for example Alam et al. (2020) and the many references therein. In contrast, only few studies have actually focussed on the aerodynamic behaviour of rounded square-section prisms at higher Reynolds numbers. So were Delany and Sorensen (1953) and Polhamus (1958) one of the first who studied the effect of edge roundness on the aerodynamic loading on 2D rounded square-section prisms at $\alpha = 0°$ in a cross-flow up to Reynolds numbers of $Re_D = 2 \times 10^6$. For this angle of incidence, they reported that an increase in r/D – where r equals the dimensional cross-sectional edge radius of the prism – resulted in the appearance of the critical Reynolds-number flow regime and in lower drag forces in the following supercritical Reynolds-number flow regime. In addition, they observed a shift of the critical flow regime towards lower Reynolds numbers for larger values of r/D. The experimental and numerical results for square-section prisms with $r/D = 0$ and 0.167 at $Re_D = 10^4$ and 10^6 by Tamura et al. (1998) proved that a decrease as large as 60% in

drag could be obtained by applying an edge roundness. In a follow-up experimental study at a fixed Reynolds number of 3×10^4 they observed that the rounded square-section prism experienced not only lower drag coefficients and higher Strouhal numbers at all angles of incidence between −5° and 30°, but that the lift fluctuations could also be reduced by about 50% compared to the values for the sharp-edged square-section prism at small angles of incidence (Tamura and Miyagi, 1999). The critical angle at which both the slope of the $C_L(\alpha)$ curve changed from negative to positive and the Strouhal number reached its maximum value, shifted from 12° for prisms with $r/D = 0$ to 5° for those with $r/D = 1/6$ and was related to an earlier reattachment of the separated shear layer on the side face exposed to the wind. Similar conclusions were drawn in Carassale et al. (2013, 2014) for two-dimensional square-section prisms with edge roundness values of $r/D = 0$, 1/15, and 2/15 in the Reynolds-number range of 1.7×10^4–2.3×10^5. Their surface pressure data at the prism's mid-section demonstrated that around $\alpha = \alpha_{cr}$, being 12°, 7°, and 5° for $r/D = 0$, 1/15, and 2/15, respectively, an increase in the suction near the leading edge of the side face exposed to the wind and a decrease close to its trailing edge occurred. Hence, this proved the formation of a separation bubble through reattachment of the free shear layer on this surface. A further increase in angle of incidence led to a shrinkage of the length of this separation bubble towards the windward edge, in agreement with the observations by Huang et al. (2010) for a square-section prism with sharp edges. The latter authors subscribed this behaviour to the steady movement of the reattachment point towards the leading edge of this side face with increasing α up to an angle of $\alpha = 45°$.

1.3. Objective of the present study

The smaller mean drag forces, higher Strouhal numbers, and lower lift fluctuations of 2D rounded square-section prisms at moderate Reynolds numbers compared to their sharp-edged counterpart, as well as a distinct dependency of their values on the Reynolds number are all induced by the relief of the fixed primary (and secondary, in the case of a free shear layer reattachment) boundary layer separation points. Their meandering along the partially rounded edges gives rise to a smaller lateral spread of the free shear layers above both side faces of the prism. The free shear layer that is present above the side face which is turned into the oncoming flow with increasing incidence angle is in that way enabled to reattach close to trailing edge of that side face already at relatively small angles of incidence (Carassale et al., 2014). The larger the value of the edge roundness, the more the critical incidence angle shifts to a lower value. This is also the main cause of the distinct reduction of the maximum possible transverse or rotational galloping amplitude of rounded square-section prisms in comparison to their sharp-edged counterpart at a certain common reduced velocity (e.g. Carassale et al. (2013)). In addition, the combination of a weaker lateral spread of the two free shear layers and the occurrence of a flow reattachment at smaller incidence angles leads to a reduction in the effective aerodynamic blockage ratio, and a decrease of the width of the wake. The latter induces then again a weaker interaction of the free shear layers in the region directly adjacent to (i.e. downstream of) the prism's base and thus a lowering of the mean suction force on the base face(s) of the prism (Tamura et al., 1998; Carassale et al., 2014).

Even to this date, little is known about the influence of the angle of incidence on the time-averaged and fluctuating loading on 2D rounded square-section prisms in a steady and uniform cross-flow at very-high Reynolds numbers of $\mathcal{O}(10^6)$ – $\mathcal{O}(10^7)$. The same applies to the susceptibility of such prisms to transverse or rotational galloping for this range of Reynolds numbers. This obvious lack of experimental and numerical data is actually quite surprising, as it can lead to serious problems for flexible or flexibly-mounted prismatic structures in various engineering fields at those full-scale Reynolds numbers.

To address those open points, the present experimental wind tunnel study focuses on the systematic analysis of the (un)steady forces and pitch moment that act on a slightly rough square-section prism with rounded edges of $r/D = 0.16$ for cross-flow Reynolds numbers between 1×10^5 and 8.0×10^6. Emphasis is furthermore put on the characteristics, i.e. strength and frequency, of the shed eddies. For that purpose, the time-averaged surface pressure distribution at the mid-section of the prism, the experienced mean base pressure coefficient C_{pb}, the sectional mean pitch moment coefficient C_m, the spanwise-integrated time-averaged and fluctuating fluid loads (C_D, C_L, C'_D, C'_L), and the Strouhal number St_L were all measured simultaneously. While the mean sectional pitch moment was calculated using the mean surface pressure distribution, all other aerodynamic coefficients and the Strouhal number were measured using two piezoelectric platform dynamometers. In addition to the Reynolds number, which covered the Reynolds-number flow regimes from subcritical to transcritical, the angle of incidence α of the prism was selected as the second governing parameter. The latter was varied between $\alpha = -45°$ and 3.25° with increments of 3.25° and 6.5°. The time-averaged fluid-dynamic forces and pitch moment were thereupon substituted into the classical linearised quasi-steady transverse and rotational galloping models to analyse not only the susceptibility of the prism to both motion-induced vibrations, but also the range(s) of Reynolds numbers in which those two aeroelastic instabilities could potentially occur.

2. Experimental approach

The experiments were performed in the closed-circuit High-Pressure Wind Tunnel, a unique test facility in which the air can be pressurised up to $p_0 = 10$ MPa to achieve maximum Reynolds numbers of 10^7 (based on the width D of the square-section prism) at model scale in a low subsonic free-stream of $U_\infty \leq 35$ m/s ($M_\infty \leq 0.1$). The test section has a square cross-section of 0.6×0.6 m^2 and measures 1 m in length. Free stream turbulence intensities ($T.I.$) in the test section and the relative dynamic pressure variation across the working section at the prism's position were below 0.8% and 0.3%, respectively.

The "infinite" square-section prism has a span of $L = 0.6$ m and common side lengths of $D = 0.06$ m, resulting in an aspect ratio of $AR = L/D = 10$, see Fig. 2. The prism was fabricated through the assemblage of two partially hollow stainless steel half models. Both half models were joined together with multiple screws and the four spanwise edges were thereupon rounded to obtain non-dimensional edge curvatures of $r/D = 0.16$ (Fig. 2). After a thorough polishment of all four lateral faces to eliminate possible geometrical imperfections, they were covered with a plasmatic metal coating to obtain a Gaussian distributed non-dimensional equivalent sand-grain surface roughness – based on the algorithm by Adams et al. (2012) – of $k_s/D = 4.5 \times 10^{-4} \pm 2 \times 10^{-5}$. The purpose of the applied surface roughness was to a simulate a light colonisation of the outer surfaces of foundation elements of offshore constructions, such as floating and bottom-fixed renewables and oil and gas production platforms, by hard marine fouling (e.g. oysters, tubeworms, and mussels) after a certain residence time in the ocean (Forteath et al., 1982; Langhamer et al., 2009; Kerckhof et al., 2010; Fitridge et al., 2012; Theophanatos, 1988). In a previous experimental study by van Hinsberg et al. (2017), performed in the same wind tunnel and at equal flow conditions, unique flow phenomena could be observed on smooth (i.e. $k_s/D = 4.5 \times 10^{-6}$) square-section prisms with various edge roundness values for $\alpha = 0°$, −22.5°, and −45°. In an experimental follow-up study on the effect of the roughness height on a square-section prism with rounded edges of $r/D = 0.16$ it was proven that an increase in this value by a factor of 100 to $k_s/D = 4.5 \times 10^{-4}$ (hence, from smooth to slightly rough) has only a marginal effect on the fluid-dynamic characteristics of the prism, such as the experienced time-averaged and fluctuating loads, the eddy shedding frequency, and the mean wake profile, in the sub- to supercritical Reynolds-number flow regimes (van Hinsberg, 2021a). The additional turbulence generated by the surface roughness

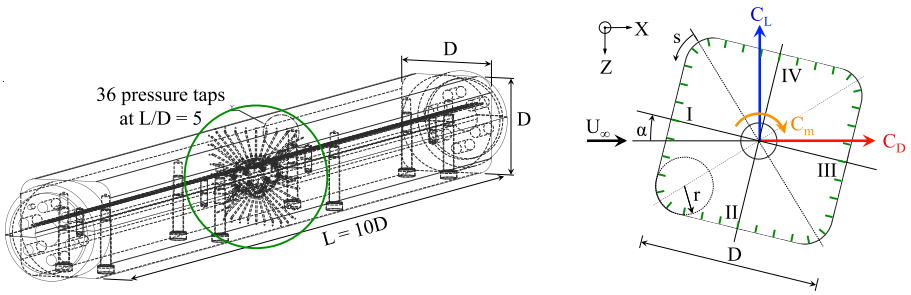

Fig. 2. Wind tunnel model and definition of the positive spanwise-integrated aerodynamic force vectors, sectional pitch moment coefficient, incidence angle, and surface coordinate s, as well as the numeration of the side faces of the prism (*I-IV*) and the locations of the 36 pressure taps (green short lines) at the prism's mid-section at $L/D = 5$.

of $k_s/D = 0.045\%$ is thus still ineffective in triggering the laminar-turbulent transition at those Reynolds numbers. This demonstrates that the laminar boundary layer is stable in these flow regimes and its thickness is such that the tops of the roughness elements do not yet extend into regions of higher velocity within the boundary layer or even pierce the boundary layer. Similar conclusions were drawn by Fage and Warsap (1929) and Achenbach and Heinecke (1981) based on the measured mean drag coefficient and Strouhal number of smooth and roughened circular cylinders with mean relative surface roughness values as high as $k/D = 2\%$–3%.

Thirty-six static pressure taps, each with a diameter of 0.3 mm were arranged in a staggered and equally spaced configuration along the model's mid-span cross-section at $y/D = 5$. They were connected through small stainless steel and plastic polyester tubes to a temperature-compensated electronic differential pressure measurement unit, having a range of ±100 kPa and a 0.15% uncertainty in the full scale. Their positions on the prism surface are given by the non-dimensional circumferential coordinate s/D with $s = 0$ at the middle of the rounded edge between the faces *I* and *IV* (Fig. 2). The staggering of the pressure tap holes was achieved by shifting each pressure tap hole in spanwise direction by a relative amount of ±1.65 mm ($\Delta y/D = \pm 0.0275$) with respect to its closest neighbours. In that way, an interference of the local flow over a tap hole by the wakes generated by the pressure holes located upstream was avoided. Based on the mean surface pressure distribution, obtained with an uncertainty below ±150 Pa (= 0.15% FS), the mean sectional pitch moment coefficient C_m could be calculated:

$$C_m = \frac{1}{D^2}\int_s C_p n_X r ds = \frac{1}{D^2}\sum_{i=1}^{36} C_{p,i} n_{X,i} r_i ds_i \tag{2}$$

where $ds_i = (s_{i+1} - s_{i-1})/2$ with s_i the circumferential position of pressure tap i measured along the peripheral of the prism according to Fig. 2, n the local normal vector on the surface of the prism at the position of pressure tap i, X the downstream directed axis with respect to the centre of the prism, r_i the distance from the longitudinal centre axis up to the position of pressure tap i, and $C_{p,i}$ the pressure coefficient at the pressure tap i, defined as $C_{p,i} = (p_i - p_\infty)/q_\infty$ with p_i the measured static pressure at pressure tap i, p_∞ the static pressure of the free-stream flow, and q_∞ the free-stream dynamic pressure. The mean base pressure coefficient C_{pb} was determined by taking the average of the pressure coefficient values of multiple surface pressure taps as listed in Table 1. The dynamic calibration of the static pressure taps showed an upper cut-off frequency of about 860 Hz.

The prism was mounted horizontally in the test section and spanned the complete test-section width between both vertical side walls. Labyrinth seals were used to minimise the amount of flow leakage through the small ring gaps between the model and the side walls. Both model ends were connected to rigid piezoelectric platform dynamometers to obtain the time-dependent global, i.e. spanwise integrated lift $L(t)$ and drag $D(t)$ forces on the model with an uncertainty below 2%. The calculated global time-averaged lift and drag coefficients are

Table 1
Range of surface pressure taps per angle of incidence used for the calculation of the mean sectional base pressure coefficient C_{pb}.

Incidence angle (α)/°	Total number of used pressure taps	Position (s/D) of first tap	Position (s/D) of last tap
3.25	18	1.81	3.57
0	9	1.91	2.74
−3.25	18	1.09	2.85
−6.5	18	1.09	2.85
−9.75	17	1.09	2.74
−13	17	1.09	2.74
−19.5	17	1.09	2.74
−25.5	18	0.98	2.74
−32	18	0.98	2.74
−38.5	18	0.98	2.74
−45	16	2.02	3.57

defined as $C_L = \overline{L(t)}/(q_\infty DL)$ and $C_D = \overline{D(t)}/(q_\infty DL)$ with $\overline{L(t)}$ and $\overline{D(t)}$ the mean values of, respectively, the recorded time series of the lift and drag forces. The power spectral densities (PSD) of the fluctuations of the lift force were used to determine both the main peaks that are associated with the eddy shedding process, and the corresponding shedding frequencies f_L. The resulting Strouhal numbers are defined as $St_L = f_L D/U_\infty$.

In a previous wind tunnel study by van Hinsberg et al. (2018) the effect of the limited aspect ratio of $L/D = 10$ on the two-dimensionality of the flow over the prism, and thus on the measured global aerodynamic loads was examined through surface-oil visualisations. It was proven that only in a small region from each wind tunnel sidewall up to about $y/D = 0.6$–0.9 in cross-flow direction a three-dimensional flow over the prism is present. Because in the current test setup the surface pressure taps are located at the mid-span cross-section of the prism (Fig. 2), the pressure data – and the sectional pitch moment derived therefrom – are obtained in a strictly two-dimensional flow.

Eleven angles of incidence between $\alpha = -45°$ and $+3.25°$, with increments of 3.25° and 6.5° at an accuracy of $\Delta\alpha = \pm 0.03°$, were selected and investigated. Since the prism was rotated in counter-clockwise direction along its centre axis, the majority of the investigated angles of incidence are designated hereafter as "negative", in accordance with the aerodynamic angle convention. The geometric wind tunnel blockage ratio varied between 0.10 ($\alpha = 0°$) and 0.13 ($\alpha = -45°$). The formulas by Allen and Vincenti (1944) and Roshko (1961) were applied to the measured free-stream velocity, the drag, and the pressure coefficients to correct for wall interference effects, resulting in maximum corrections in the order of 10%. This relatively high geometric blockage ratio may raise the question to what extend this parameter influences the incidence-angle-dependent aerodynamics of the current prism. In van Hinsberg (2021b) the experimentally obtained mean drag and lift coefficients and the Strouhal number of a sharp-edged square-section prism in cross-flow at equal boundary conditions (i.e. wind tunnel, measurement technique, and model aspect ratio) as the currently investigated rounded square-section prism were compared

to those values obtained by others through wind tunnel experiments and numerical simulations. When focussing in particular on the data published by Carassale et al. (2014), as those values were also acquired with piezoelectric platform dynamometers, it was shown that only marginal differences of less than 3% exist between their blockage-uncorrected values for C_D, C_L, and St_L at $\alpha = 0°$, 22.5° (interpolated between $\alpha = 20°$ and 25°), and 45° and the ones obtained in the High-Pressure Wind Tunnel facility, the latter having been corrected for the geometric wind tunnel blockage. Note, that the difference in Reynolds number, hence, $Re_D = 3.7 \times 10^4$ (Carassale et al., 2014) compared to $10^5 \leq Re_D \leq 10^7$ (van Hinsberg, 2021b), can be ignored, as for $Re_D \geq 10^4$ the flow around the sharp-edged square-section prisms is situated in the *shear layer transition II* regime and is thus highly Reynolds-number independent (Bai and Alam, 2018). A correction of the data of Carassale et al. (2014) for their geometric wind tunnel blockage ratio of only 2.5% at $Re_D = 3.7 \times 10^4$ reduces this difference to values below 1%. This high degree of equality in the values of the aerodynamic coefficients for completely different geometric wind tunnel blockage ratios clearly implies the absence of a coupling between the geometric blockage effect and the angle of incidence on the aerodynamics of this prism in the High-Pressure Wind Tunnel facility. Moreover, for square-section prisms the flow field around the sharp-edged model is characterised by the largest lateral spread of the free shear layers along both side faces and thus induces the highest possible aerodynamic blockage. On the basis of these points, it can be argued that for the current rounded square-section prism, a coupled influence on the aerodynamics by both the geometric blockage and angle of incidence is therefore also not to be expected.

Per measurement point a constant integration time of $T = 30$ s was chosen for all recorded signals, as it was demonstrated in a previous study by van Hinsberg et al. (2018) that this time span was sufficient to obtain well-converged time-averaged and fluctuating aerodynamic coefficients. The spanwise-integrated aerodynamic forces were thereby scanned with a sampling frequency of $f_{scan} = 5$ kHz at a resolution of 16 bit.

3. Experimental results

3.1. Time-averaged global and sectional aerodynamic coefficients

Fig. 3 shows the variations of C_D, C_L, C_m, and C_{pb} with respect to the angle of incidence for twenty Reynolds numbers between $Re_D = 2.0 \times 10^5$ and $Re_D = 6.0 \times 10^6$, hence spanning the subcritical to transcritical Reynolds-number flow regimes. Focussing first of all on the dependency of the time-averaged global drag coefficient on the angle of incidence at constant Reynolds number, it can be observed in Fig. 3a that for a Reynolds number up to $Re_D = 3.0 \times 10^5$, i.e. up to the end of the subcritical Reynolds-number flow regime, a decrease in C_D takes place as the incidence angle goes from $\alpha = 0°$ to the more negative value of $\alpha = -6.5°$. At the latter of those two bounding incidence angles, a sign inversion of the slope of the $C_D(\alpha)$ curve from positive to negative occurs, which is followed by a steady increase of C_D while continuing to more negative angles of incidence and a flattening of the $C_D(\alpha)$ curve for $\alpha \to -45°$. It can thus be stated that the model angle of $\alpha = -6.5°$ either corresponds or lies close to the critical angle of incidence at which the upper free shear layer steadily reattaches to the side face *IV* in the vicinity of its downstream-directed rounded edge and the flow state thus switches from the *perfect separated* flow regime to the *reattachment* or *separation* flow regime. This value for α_{cr} at (low) subcritical Reynolds numbers is only slightly higher than $\alpha_{cr} = 5°$ measured by Carassale et al. (2014) for a 2D rounded square-section prism with $r/D = 2/15$ at a subcritical Reynolds number of $Re_D = 2.7 \times 10^4$ in a smooth cross-flow with a free stream turbulence intensity of $T.I. = 0.2\%$. Although they used a square-section prism with $r/D = 0.167$ – hence, with a near equal edge roundness value as in the current experiment – (Tamura and Miyagi, 1999) also obtained a somewhat lower critical incidence angle of $\alpha_{cr} = 4°$–5° in laminar free stream flow conditions ($T.I. < 0.3\%$ and $Re_D = 3.0 \times 10^4$).

Interestingly, Fig. 3a and 3b show that for Reynolds numbers larger than 3.5×10^5 two distinct developments of the mean global drag coefficient with incidence angle can be distinguished. In the one case, the steady increase in C_D starts straight away from $\alpha = 0°$, before levelling off at more negative incidence angles and finally reaching a relatively constant upper plateau around $\alpha = -32°$. In the other case, this increase of C_D with angle of incidence is preceded by a plateau with low constant values of C_D that is limited to $\alpha = -3.25°$ or $\alpha = -6.5°$, dependent on the specific Reynolds number. Because of the lack of a singular point of the corresponding $C_D(\alpha)$ curve at each of those Reynolds numbers, no exact appointment of the critical angle of incidence can be derived from their trends. The curve at $Re_D = 3.5 \times 10^5$ in Fig. 3a is special in that it can be interpreted as a transition between the two main trends at low negative angles of incidence: between $\alpha = 0°$ and −3.25° the drag slope is negative and thus consistent with the curves for $Re_D \geq 4 \times 10^5$, while $dC_D/d\alpha > 0$ in the range of $\alpha = -3.25°$ to −6.5° and thus follows the trend of the curves for Reynolds numbers below 3.5×10^5.

Although the behaviour of the mean sectional base pressure coefficient C_{pb} is generally directly coupled to the mean global drag coefficient, the two exact opposite trends of C_D with increasing Reynolds number in the range of $\alpha = -6.5°$–0° cannot be seen in the behaviour of C_{pb} in the Figs. 3g and 3h. In comparison to C_D, a somewhat wider spreading of the values of the mean sectional base pressure coefficient can furthermore be observed for $Re_D = 4 \times 10^5$–8×10^5 at those angles of incidence. This spreading is caused by the relatively deep and bright dip in the corresponding $C_{pb}(Re_D)$ curves for $\alpha = -3.25°$ to −13°. The deviation of the trends of the $C_{pb}(\alpha)$ curves for $Re_D = 5.5 \times 10^5$ and 6.0×10^5 at $|\alpha| \geq 38.5°$ from those at all other Reynolds numbers is then again in close agreement with the results obtained for C_D.

The curves of the time-averaged global lift and sectional pitch moment coefficients as function of the incidence angle, presented in the Figs. 3c and 3d and in the Figs. 3e and 3f, respectively, possess two main trends that appear alternately and are divided at each crossover by a transition curve at a certain Reynolds number. For relatively low Reynolds numbers up to about 4.0×10^5, C_L shows a steady increase for negative incidence angles from $\alpha = 0°$ down to $\alpha_{cr} \approx -6.5°$, see Fig. 3c. This is followed by a gradual decrease with a slope $dC_L/d\alpha$ that is near to independent of the Reynolds number, a change to a negative mean global lift coefficient between $\alpha = -25.5°$ and −32°, and a moderate recovery towards $C_L = 0$ for $\alpha \to -45°$. A relatively similar, but opposite behaviour is found for C_m for $Re_D \leq 3.5 \times 10^5$ in Fig. 3e. For incidence angles down to $\alpha = -6.5°$, C_m reduces sharply. This decrease is either followed directly by a gradual and steady recovery of C_m towards $C_m = 0$ at $\alpha = -45°$ (for $Re_D = 2.0 \times 10^5$ and 2.5×10^5), or first by an intermediate and short plateau with a rather constant value of C_m for incidence angles between −6.5° and −13° (i.e. for $Re_D = 1.0 \times 10^5$, 3.0×10^5, and 3.5×10^5) before the recovery towards $C_m = 0$ at $\alpha = -45°$ sets in as well.

At the first transitional Reynolds number around $Re_D = 4.0 \times 10^5$–4.5×10^5, a change in the absolute values of both aerodynamic coefficients is seen to occur, for C_L at angles of incidence between $\alpha = 0°$ and −19.5°, while for C_m this range of incidence angles is limited to $\alpha = -6.5°$–0°. This transition is furthermore much clearer for the former than for the latter aerodynamic coefficient.

In the following range of Reynolds numbers that prolongs up to $Re_D = 7.5 \times 10^5$ the $C_L(\alpha)$ and the $C_m(\alpha)$ curves have swapped trends and therefore keep their mirrored image. Down to an incidence angle of either $\alpha = -6.5°$ (for the first half of this Reynolds-number range up to $Re_D = 6.0 \times 10^5$) or $\alpha = -3.25°$ (for the second half up to $Re_D = 7.5 \times 10^5$) the global lift coefficient shows a strong negative trend, while the sectional pitch moment coefficient becomes increasingly positive in the exact same range of incidence angles. This is directly followed by a steep recovery of C_L to values that lie close

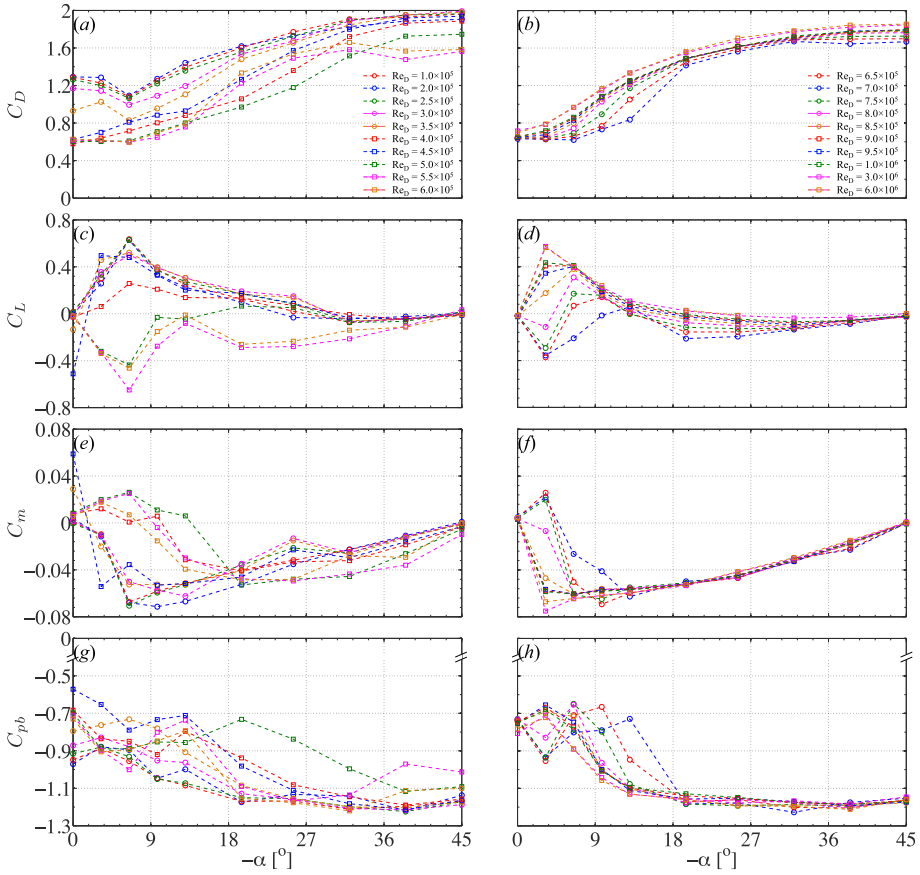

Fig. 3. Time-averaged spanwise-integrated drag coefficient ((*a*) and (*b*)), time-averaged spanwise-integrated lift coefficient ((*c*) and (*d*)), mean sectional pitch moment coefficient ((*e*) and (*f*)), and mean sectional base pressure coefficient ((*g*) and (*h*)) as a function of the angle of incidence in the range of Reynolds numbers of 1.0×10^5–6.0×10^5 (left column) and 6.5×10^5–6.0×10^6 (right column).

to $C_L = 0$. At several Reynolds numbers this recovery is additionally combined with a sign reversal of C_L. In contrast, the $C_m(\alpha)$ curves show either a steady and moderate (Fig. 3e) or a steep (Fig. 3f) decrease for more negative incidence angles, whereby a sign change appears at all Reynolds numbers. Interestingly, for $|\alpha| \geq 13°$–$19.5°$ the behaviour of each of those $C_m(\alpha)$ curves clearly resembles that one discussed above for $Re_D \leq 4.0 \times 10^5$. Regarding the lift coefficient, the majority of the curves shows a wide valley in this range of incidence angles that ends at approximately $C_L = 0$ at $\alpha = -45°$.

For all Reynolds numbers above the second common transitional Reynolds number of $Re_D = 8.0 \times 10^5$, the individual curves of both aerodynamic coefficients obtain once again the exact same shape as previously discussed for subcritical Reynolds numbers.

3.2. Fluctuating global aerodynamic coefficients

The dependency of the fluctuating global force coefficients, $\sqrt{(\overline{C_D'^2})}$ and $\sqrt{(\overline{C_L'^2})}$, on the incidence angle is presented in Figs. 4a to 4d for the same twenty Reynolds numbers in the range of $Re_D = 1 \times 10^5$–6×10^6. At large absolute incidence angles, there is a striking resemblance between the behaviour of both fluctuating coefficients at each Reynolds number. Distinct differences in the trends are then again obtained at combinations of small absolute incidence angles and relatively low Reynolds numbers up to $Re_D = 3.0 \times 10^5$, i.e. up to the point at which the crossover from the subcritical into the critical Reynolds-number flow regime takes place. At subcritical Reynolds numbers, the value of $\sqrt{(\overline{C_D'^2})}$ increases steadily with decreasing angle of incidence, levels off at intermediate negative incidence angles, and reaches a plateau with relatively constant values of $\sqrt{(\overline{C_D'^2})} = 0.16$–$0.21$ for $\alpha \to -45°$, Fig. 4a. By contrast, the curves of the fluctuating lift in Fig. 4c are characterised by an initial sharp drop in the range of $\alpha = -6.5°$–$0°$. Their further course down to $\alpha = -45°$ has then again a similar trend as previously described for $\sqrt{(\overline{C_D'^2})}$.

The transition around $Re_D = 3.5 \times 10^5$ is also visible in the trends of both fluctuating global force coefficients. It is reflected in the presence of an additional bright valley between $\alpha = -13°$ and $0°$ with minimum values of $\sqrt{(\overline{C_D'^2})} = 0.03$ and $\sqrt{(\overline{C_L'^2})} = 0.05$ around $\alpha = -6.5°$. From this Reynolds number upward, several trends can be distinguished at low to intermediate absolute incidence angles. At $Re_D = 4.0 \times 10^5$ and 4.5×10^5, both fluctuating global force coefficients possess approximately constant values for incidence angles down to $\alpha = -13°$. A slight increase in the Reynolds number to $Re_D = 5.0 \times 10^5$ leads to the appearance of a second plateau in both the $\sqrt{(\overline{C_D'^2})}(\alpha)$ and $\sqrt{(\overline{C_L'^2})}(\alpha)$ curve. The first of the two plateaus at approximately $\sqrt{(\overline{C_D'^2})} = 0.06$ and $\sqrt{(\overline{C_L'^2})} = 0.11$ starts at $\alpha = 0°$ and spreads down to $\alpha = -6.5°$. The following second plateau continues to angles of incidence as low as $\alpha = -19.5°$ for the fluctuating global drag coefficient and even to $\alpha = -25.5°$ for the fluctuating lift coefficient. Interestingly, for both coefficients the two plateaus possess a similar behaviour with a further increase in Reynolds number. It is characterised by a continuous reduction in the range of covered incidence angles towards a single point at $\alpha = 0°$ (1st plateau) and $\alpha = -3.25°$ (2nd plateau), the latter being obtained at $Re_D \geq 8.5$–9.0×10^5. While the Reynolds number thus has a significant effect on the shape of the curves at low to intermediate absolute angles of incidence, the trends of the curves gradually converge to a single one for $Re_D \geq 4.0 \times 10^5$

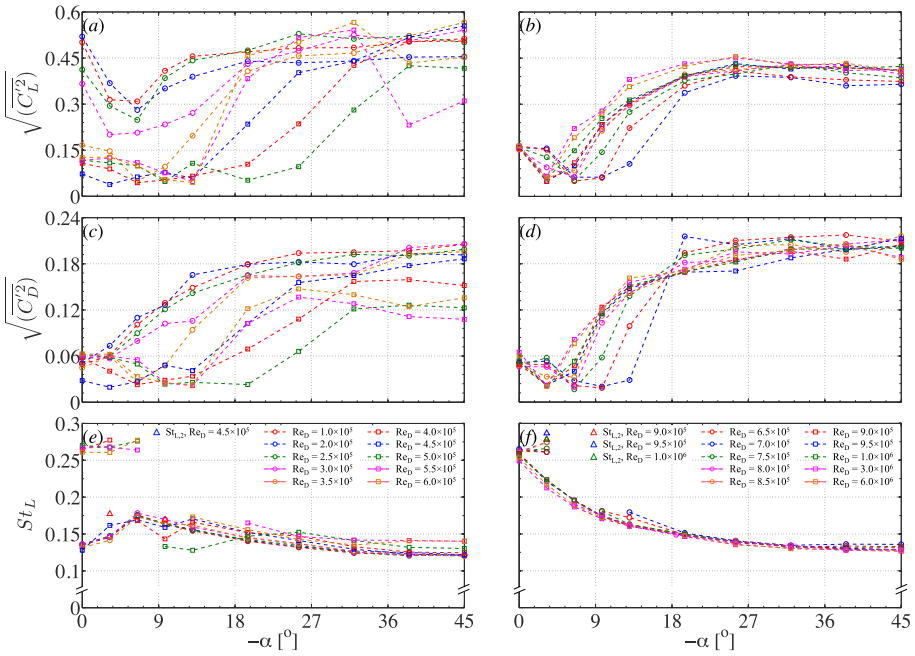

Fig. 4. Fluctuating spanwise-integrated lift coefficient ((*a*) and (*b*)), fluctuating spanwise-integrated drag coefficient ((*c*) and (*d*)), and Strouhal number ((*e*) and (*f*)) as a function of the angle of incidence in the range of Reynolds numbers of 1.0×10^5–6.0×10^5 (left column) and 6.5×10^5–6.0×10^6 (right column). The dominant Strouhal numbers in (*e*) and (*f*) are indicated by circles, whereas the triangles belong to the secondary peaks of the PSDs in Fig. 5.

at higher absolute incidence angles. It possesses a steep increase with increasing absolute incidence angles up to a final plateau with high values of $\sqrt{(\overline{C_D'^2})}$ and $\sqrt{(\overline{C_L'^2})}$. For both coefficients, the height of this plateau strongly depends on the value of the Reynolds number (i.e. the corresponding Reynolds-number flow regime).

3.3. Strouhal number and power spectra

Based on their overall trend, the curves of the Strouhal number versus the incidence angle in Fig. 4e and 4f can be split up into two parts. The first one is characterised by clear changes in St_L with varying Reynolds number for incidence angles in the range of $\alpha = -6.5°$–$0°$. The second part, which is covered by all remaining incidence angles, consists of a near-perfect agreement in both the course of the different curves and the actual values of the Strouhal number among all Reynolds numbers.

The second of those two branches, i.e. for $|\alpha| \geq 6.5°$, is defined by a gradual decrease of St_L that ends in a levelling-off towards an asymptotic value of $St_L = 0.12$–0.14 at $\alpha = -45°$. This trend is confirmed by the underlying power spectra of the unsteady lift force at six Reynolds numbers in the range of $Re_D = 2.0 \times 10^5$ to 6.0×10^6, presented in Fig. 5. Starting from $\alpha = -9.75°$ (magenta curves in the upmost and third row of Fig. 5), a progression towards more negative incidence angles induces a wandering of the single dominant and relatively broad peak at each Reynolds number towards lower non-dimensional shedding frequencies. The PSDs furthermore show that a continuous increase in Reynolds number from sub- to transcritical has merely a small effect on the exact location of this peak, i.e. the value of the Strouhal number. By contrast, the height of the main peak is clearly affected by the Reynolds number. While a change in incidence angle from $\alpha = -6.5°$ towards $\alpha = -45°$ induces at the majority of the studied Reynolds numbers hardly any changes in the peak's height – with the exception of $Re_D = 4.5 \times 10^5$ (Fig. 5e) and 5.0×10^5 (Fig. 5f) – an increase of two orders of magnitude in the peak's height is observed between the lowest and the highest Reynolds number.

The first branch that spans the angles of incidence from $\alpha = 0°$ to $-6.5°$ shows an exact opposite situation: the value of the Strouhal number now depends to a high degree on the Reynolds number, while the height of the main peak in the corresponding PSDs in Fig. 5 is relatively constant for all Reynolds numbers. Based on the shape of the curves and the values of St_L in Fig. 4e and 4f, three sub-branches can be differentiated.

The first sub-branch is present up to medium to high critical Reynolds numbers of 4.0×10^5. The $St_L(\alpha)$ curve shows a sharp increase from $St_L = 0.14$ at $\alpha = 0°$ up to its absolute maximum of $St_L = 0.18$ at $\alpha_{cr} \approx -6.5°$, see Fig. 4e. The single dominant peak of the PSDs in this Reynolds-number range appears at similar non-dimensional shedding frequencies, has a similar height, and is rather narrow (Fig. 5a and 5c). Around the critical angle of incidence, a singular point exists in the Strouhal-number curve as the slope $dSt_L/d\alpha$ changes sign, whereupon the curve starts its second trend line towards $\alpha = -45°$ (Fig. 4e).

The curve at $Re_D = 4.0 \times 10^5$ shows small fluctuations between $\alpha = 0°$ and $\alpha = -13°$ that can be seen as an indication for the imminent transition from the first to the second sub-branch. The latter is defined by high, constant Strouhal numbers of $St_L = 0.26$–0.28. For Reynolds numbers that belong to the high critical (i.e. $Re_D = 4.5 \times 10^5$) and upper transition (hence, $Re_D = 6.5 \times 10^5$–8.5×10^5) Reynolds-number flow regimes this branch is limited to $|\alpha| \leq 3.25°$. For all supercritical Reynolds numbers it continues to $|\alpha| = 6.5°$ instead. Subsequently, each of these curves experiences a significant drop in St_L down to the second overall trend line. A limited range of incidence angles in which no frequency peak associated with the regular eddy shedding could be identified precedes this drop. This latter range is denoted hereafter as $\Delta\alpha_{w/oSt}$, the length of which varies with Reynolds number. At $Re_D = 4.5 \times 10^5$ and 5.0×10^5 the jump in St_L takes place in between $\alpha = -3.25°$ and $-6.5°$ (hence, two neighbouring investigated incidence angles), which leads to $\Delta\alpha_{w/oSt} = 0°$. At both Reynolds numbers, the flow jumps from the supercritical back into the critical Reynolds-number flow regime. In addition, at the lower of these two Reynolds numbers, two Strouhal numbers appear at $\alpha = -3.25°$ and $-9.75°$, associated either with the switching of the flow around the prism back and forth between the critical and supercritical flow states ($\alpha = -3.25°$) or with the presence of two separate branches in the $St_L(Re_D)$ curve ($\alpha = -9.75°$) at this Reynolds number. At $Re_D = 5.5 \times 10^5$ the value

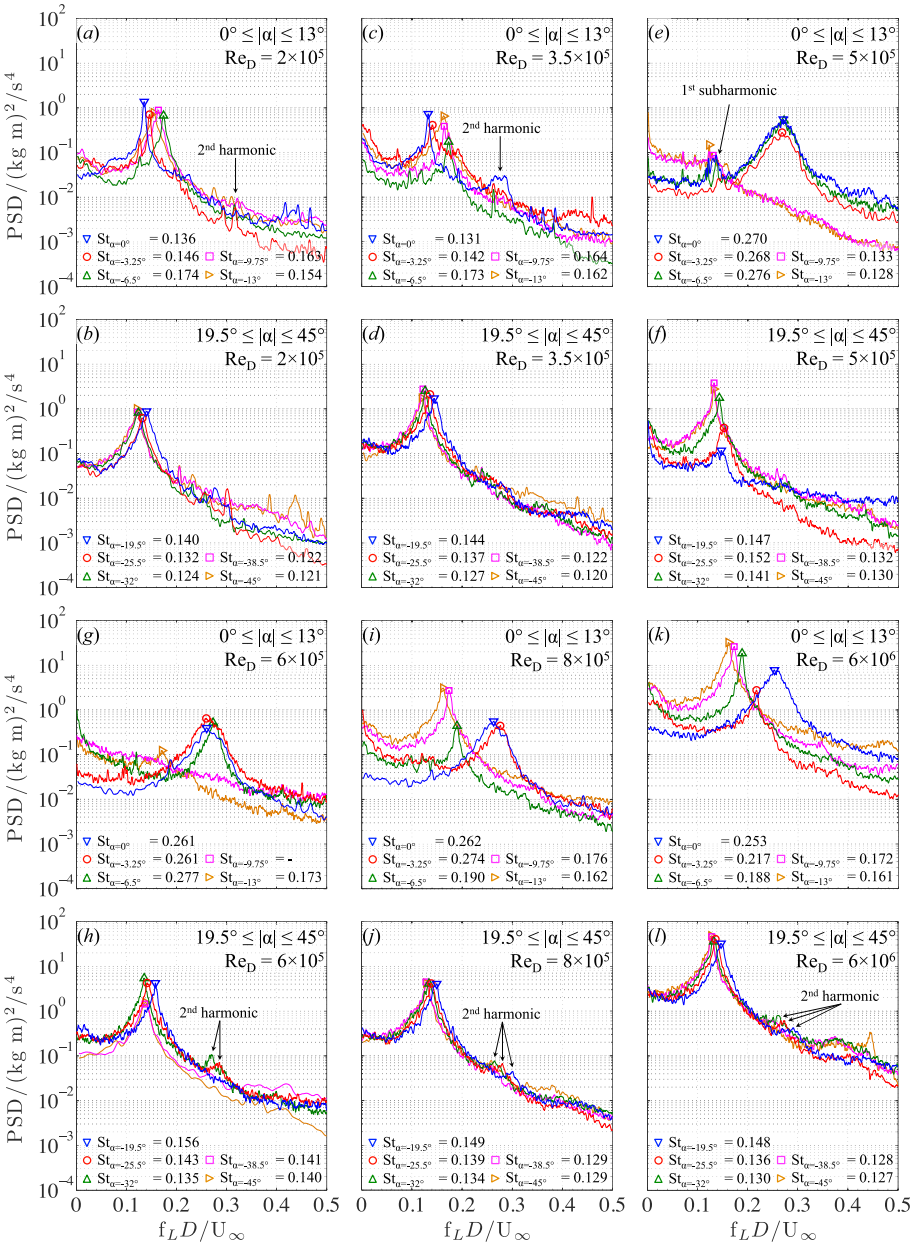

Fig. 5. Power spectral densities of the time series of the spanwise-integrated lift force on the prism for $0° \leq |\alpha| \leq 45°$ at selected Reynolds numbers between 2.0×10^5–6.0×10^6. *(a)* and *(b)*: $Re_D = 2.0 \times 10^5$; *(c)* and *(d)*: $Re_D = 3.5 \times 10^5$; *(e)* and *(f)*: $Re_D = 5.0 \times 10^5$; *(g)* and *(h)*: $Re_D = 6.0 \times 10^5$; *(i)* and *(j)*: $Re_D = 8.0 \times 10^5$; *(k)* and *(l)*: $Re_D = 6.0 \times 10^6$. The corresponding Strouhal numbers are indicated by the symbols on the curves and the numbers inside each graph.

of $\Delta\alpha_{w/oSt}$ reaches its absolute maximum of $\Delta\alpha_{w/oSt} = 13.5°$, upon which it reduces in length with further increasing Reynolds number before reaching once more its starting value of $\Delta\alpha_{w/oSt} = 0°$ around $Re_D = 8.0 \times 10^5$–8.5×10^5, i.e. at the crossover from the upper transition into the transcritical Reynolds-number flow regime. An example of the shape of the corresponding PSD curve within this limited range of incidence angles is given in Fig. 5g for $\alpha = -9.75°$ at $Re_D = 6.0 \times 10^5$. From this graph, it becomes evident that the eddy shedding (and thus VIV) is fully suppressed.

The third, and final sub-branch for $Re_D \geq 9.0 \times 10^5$ is marked by a steady decrease of the Strouhal number from $St_L = 0.25$–0.26 at $\alpha = 0°$ down to $St_L = 0.19$–0.20 at $\alpha = -6.5°$, at which point a seamless transition into the second part of the overall trend line down to $\alpha = -45°$ takes place. At $\alpha = -3.25°$, the transition from the upper transition to the transcritical Reynolds-number flow regime takes place in between $Re_D = 9.0 \times 10^5$ and 1×10^6. In this limited range of Reynolds numbers, the flow over the prism alternates between the supercritical and transcritical state, confirmed by the occurrence of two Strouhal numbers at each Reynolds number: $St_L = 0.22$ (transcritical and dominant) and $St_L = 0.28$–0.29 (supercritical and secondary).

4. Discussion

The results that have been presented in the preceding section have shown that the separate and combined variations in Reynolds number and angle of incidence have a significant effect on the time-dependent fluid dynamics of the current prism.

One issue that deserves to be scrutinised in more detail is the mean circumferential surface pressure distribution at mid-span of the prism at multiple selected Reynolds numbers in the range of $1 \times 10^5 \leq Re_D \leq 8 \times 10^6$. In the current study no flow visualisation techniques, like smoke visualisation or Particle Image Velocimetry, were applied, since their implementation inside a high-pressure environment of up to

p_0 = 10 MPa is associated with major challenges and risks. Therefore, we cannot substantiate the following discussion with detailed information on the flow field around and the wake structures behind the analysed rounded square-section prism. Nevertheless, the surface pressure distributions presented hereafter, in combination with the corresponding time-averaged and fluctuating aerodynamic forces, the mean sectional pitch moment, and the frequency and strength of the shed eddies give us an initial impression of the expected flow behaviour.

The second accent of this section is put on a possible susceptibility of the prism to 1-DoF transverse and rotational galloping within the studied range of Reynolds numbers. By using the values of the slopes of the time-averaged global lift and mean sectional pitch moment, i.e. $dC_L/d\alpha$ and $dC_m/d\alpha$, at $\alpha = 0°$ to $-9.75°$, it is shown that the linearised quasi-steady fluid-dynamic models do in fact predict a tendency to galloping, albeit in specific ranges of Reynolds numbers only that are either bounded at one or at both sides.

4.1. Mean sectional pressure distribution: effect of both governing parameters

The development of the mean sectional surface pressure distribution over the prism's mid-span with incidence angle is presented in Figs. 6 and 7 for six Reynolds numbers that are representative for the various Reynolds-number flow regimes. The first of these two figures shows the quantitative distribution of the surface pressure coefficient $C_{p,cyl}$ as a function of the non-dimensional circumferential distance s/D along the prism's peripheral (see Fig. 2). By means of a scaled vectorial representation, the second figure gives an additional qualitative impression of each of those distributions. The values of the time-averaged global drag and lift coefficients, as well as of the mean sectional pitch moment coefficient are included in the individual graphs of Fig. 7 to facilitate the correlation between the changes in surface pressures and in the resultant fluid-dynamic coefficients.

At the subcritical Reynolds number of 2×10^5, a highly symmetric mean pressure distribution with respect to the virtual horizontal line through s/D = 0.47 and 2.33 is obtained at $\alpha = 0°$ (Fig. 6a and 7a). Based on the classification by Igarashi (1984), introduced in Section 1, the flow around the prism belongs to the category of symmetric flows, i.e. the first of the two sub-categories of the perfect separated flow regime. The relatively constant negative mean pressures of $C_{p,cyl} = -1.08$ over the side faces *II* and *IV* and $C_{pb} = -0.95$ over the base (face *III*) of the prism demonstrate that after separation of the laminar boundary layer at both forward-directed rounded edges no reattachment of the free shear layers does occur on one or more of those faces. This implies, that a relatively strong deflection of the streamlines and a distinct downstream spread of the free shear layers in lateral direction along both side faces *II* and *IV* takes place, despite the presence of a rounding of the lateral edges as large as 16% of the prism's side width. The time-averaged global drag coefficient thereupon reaches a high value of $C_D = 1.29$ (Fig. 3a and 8a), while near-zero values are obtained for both the time-averaged global lift and mean sectional pitch moment coefficients (Fig. 3c and 3e).

A slight rotation of the prism to $\alpha = -3.25°$ induces only marginal changes in the mean sectional surface pressure distribution. The turning of the rounded edge between the faces *I* and *II* into the wake induces a small relocation of the boundary layer separation point to, most probably, a position slightly further downstream that leads to a light overall reduction of the suction on face *II* compared to $\alpha = 0°$. The resultant light asymmetry in the pressure distribution leads nevertheless to a pronounced time-averaged global lift coefficient of $C_L = 0.30$, the appearance of a small negative pitch moment coefficient ($C_m = -0.01$), and a small reduction of the time-averaged global drag coefficient (Fig. 8a). This proves that the flow field around the prism belongs at this angle of incidence to the asymmetric flows, i.e. the second sub-category of the perfect separated flow regime.

A doubling of the negative incidence angle to $\alpha = -6.5°$, i.e. near the critical angle, leads to a distinct asymmetry in the pressure values between both side faces *II* and *IV* (Fig. 6a and 7). A reattachment of the lower free shear layer on the lateral face *II* is still prevented at this incidence angle. The migration of the separation point of the opposite boundary layer in upstream direction, in combination with the increased proximity of the free shear layer upon separation to its corresponding side face *IV*, allow a reattachment of the free shear layer close to the trailing edge of this face. The resultant one-sided reattachment-like flow field has thereby switched from the perfect separated flow regime to the reattachment or separation flow regime. A recirculation bubble is thus formed on the upstream portion of this prism's side face, which appears in Fig. 6a and 7 as a local increase in the suction pressure, and a secondary separation of the reattached boundary layer on or near the downstream upper rounded edge. As a result of the different positions of the boundary layer separation points on the upper and lower faces of the prism, a much weaker communication of the two shear layers in the base region of the prism is expected to take place. This is projected by the absolute minimum and absolute maximum of the fluctuating global lift force and Strouhal number, respectively, at this incidence angle (Fig. 4). The mean suction pressure at the base of the prism (face *III*) thereupon decreases to $C_{pb} = -0.89$ and the time-averaged global drag coefficient reaches its absolute minimum of $C_D = 1.08$ at the current Reynolds number of $Re_D = 2 \times 10^5$ (Fig. 3a and 8a). The clear imbalance between the mean pressures in cross-flow direction below and above the prism leads to a large steady time-averaged global lift coefficient of $C_L = 0.63$ (Fig. 3c) and a negative mean pitch moment of $C_m = -0.067$ (Fig. 3e).

The wandering of the reattachment location in upstream direction along side face *IV* towards its leading edge while turning the prism to more negative incidence angles induces a shrinkage in size of the one-sided separation bubble. The latter is visible in the surface pressure distribution by a reduction of the length of the adverse pressure recovery region. The suction peak near the leading edge initially increases before reducing with every further rotation of the prism towards $\alpha = -25.5°$ (Fig. 6b and 6c, as well as Fig. 7). The area on the upper lateral face *IV* with a reattachment-like flow thus grows steadily in upstream direction, while the flow on the lower lateral face *II* remains fully separated for all angles of incidence. At $\alpha = -32°$, the pressure on the upstream half of face *IV* has becomes negative. The resemblance of the overall pressure distribution on this face with that on face *I* suggests a complete absence of the separation bubble on the former face. This implies that the boundary layer on face *I* remains attached up to its separation over the upper rounded shoulder edge. The flow field around the prism has thus switched once more, this time from the reattachment or separation flow regime to the wedge or attached flow regime. By gradually turning the prism towards $\alpha = -45°$ a migration of the stagnation point from $s/D = 0.47$ at $\alpha = 0°$ towards $s/D = 0$ at $\alpha = -45°$ takes place. During this transition, the increasing symmetry of the surface pressures between the upper and lower sides of the prism leads to a gradual decrease of both C_L and C_m to 0 at the second symmetric angle of $\alpha = -45°$. Similar to sharp-edged square-section prisms (e.g. Huang et al. (2010), Yen and Yang (2011), Sohankar et al. (2015)), the increase in the lateral spacing between the two main boundary layer separation points, located at both rounded shoulder edges, results in a wider spread in cross-flow direction of the free shear layers that have separated from those edges. In combination with an increasing geometric blockage ratio towards 0.13, a larger effective aerodynamic blockage appears. The suction force at the base of the prism becomes larger (Fig. 3g) and a higher time-averaged global drag is obtained that slowly approaches the value of $C_D = 1.96$ at $\alpha = -45°$ (Fig. 3a and 8b). The strong increase in the fluctuating global lift with incidence angle in Fig. 4c is then again most probably caused by the increased presence of the afterbody, formed by the faces *II* and *III*, while turning them into the wake. Interestingly, the values of the fluctuating global drag and the Strouhal number gradually regain at

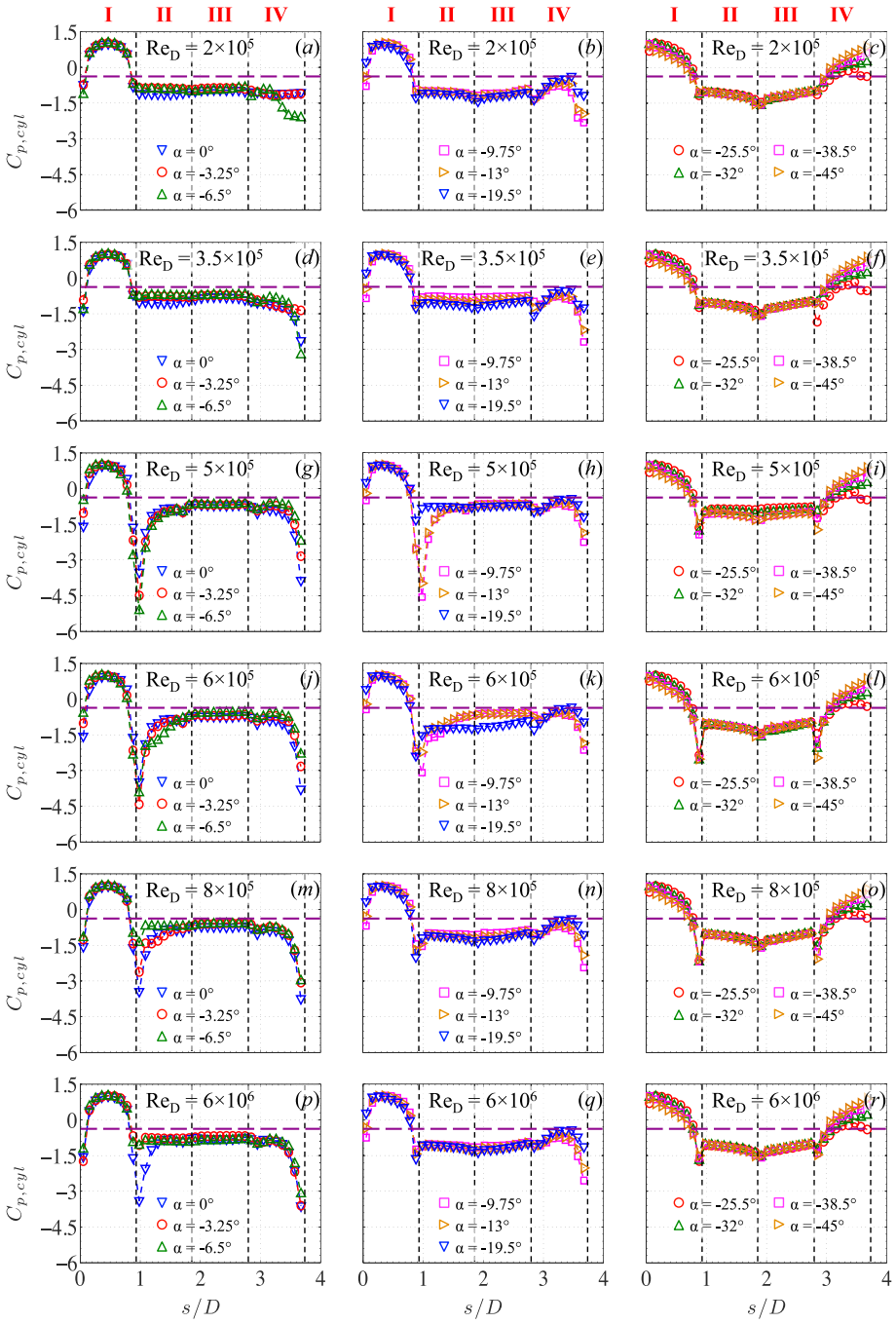

Fig. 6. Quantitative representation of the mean circumferential surface pressure distribution over the mid-span cross-section of the prism for all studied angles of incidence at selected Reynolds numbers from subcritical to transcritical. (*a*)-(*c*): $Re_D = 2.0 \times 10^5$; (*d*)-(*f*): $Re_D = 3.5 \times 10^5$; (*g*)-(*i*): $Re_D = 5.0 \times 10^5$; (*j*)-(*l*): $Re_D = 6.0 \times 10^5$; (*m*)-(*o*): $Re_D = 8.0 \times 10^5$; (*p*)-(*r*): $Re_D = 6.0 \times 10^6$. The colours correspond to the colours of the curves in Fig. 5.

$\alpha = -45°$ their initial values for $\alpha = 0°$ and are thus apparently not affected by this afterbody. This implies, that during the process of roll-up of the free shear layers in the base region behind the prism the interaction of those shear layers with the afterbody induces increasingly stronger surface pressure fluctuations in cross-flow direction at this subcritical Reynolds number.

As Re_D increases, various Reynolds-number flow regimes are passed one after another for the prism at 0° angle of incidence. At the transitional Reynolds number of $Re_D = 3.5 \times 10^5$ we are in the middle of the critical Reynolds-number flow regime with a fully-separated flow on the lower lateral face *II* and a reattachment-like flow with a small separation bubble on the upper lateral face *IV* (Fig. 6d and 7). The secondary separation of the reattached boundary layer at the downstream upper rounded edge introduces a smaller near wake (van Hinsberg, 2021a) and a lower mean suction force on the base face *III* ($C_{pb} = -0.80$, Fig. 3g). This leads to a lower time-averaged global drag force of $C_D = 0.93$ compared to 1.29 at $Re_D = 2 \times 10^5$ in the subcritical Reynolds-number flow regime (Fig. 3a and 8a).

The light asymmetry in the surface pressures between both lateral faces and the somewhat higher suction pressures over the laminar separation bubble result in a steady, but still relatively small negative time-averaged global lift and positive mean sectional pitch moment coefficient. Surprisingly, an effect of the light asymmetry in $C_{p,cyl}(s/D)$, present at $\alpha = 0°$, is noticed in the mean surface pressure distributions

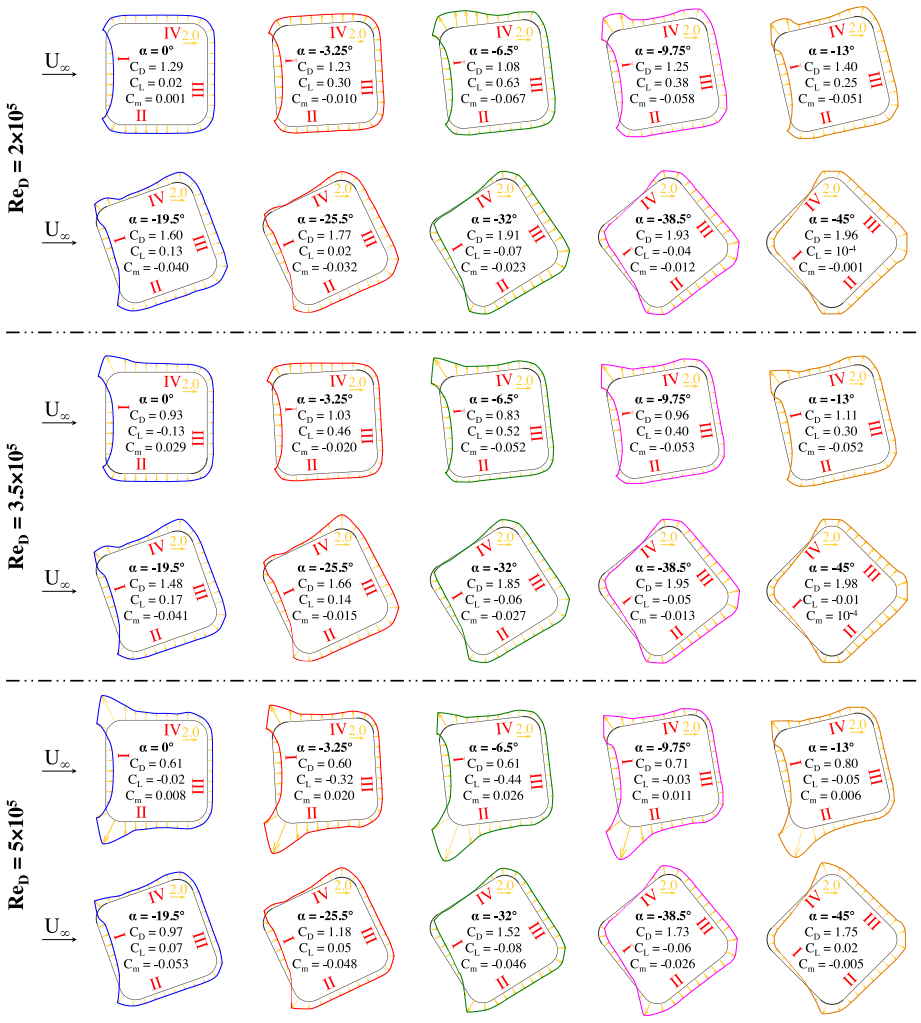

Fig. 7. Qualitative scaled vectorial representation of the mean circumferential surface pressure distribution over the mid-span cross-section of the prism for all studied angles of incidence at selected Reynolds numbers between 2.0×10^5–6.0×10^6. The colours correspond the colours of the curves in Figs. 5 and 6. First page: $Re_D = 2.0 \times 10^5$ (upper two rows); $Re_D = 3.5 \times 10^5$ (centre rows); $Re_D = 5.0 \times 10^5$ (lower two rows), second page: $Re_D = 6.0 \times 10^5$ (upper two rows); $Re_D = 8.0 \times 10^5$ (centre rows); $Re_D = 6.0 \times 10^6$ (lower two rows).

for incidence angles as far up as $|\alpha| = 25.5°$ at this specific Reynolds number. It mainly manifests itself in a light reduction of the adverse pressure recovery region (i.e. the recirculation bubble) on face *IV*, in particular at $\alpha = -6.5°$ and $-9.75°$. In addition, the higher suction peak at the windward-directed upper rounded edge at the transitional Reynolds number (Fig. 7) and the somewhat higher negative pressure in the vicinity of the secondary separation point at the trailing edge of face *IV* at $\alpha = -19.5°$ and $-25.5°$ in Fig. 6e and 6f are also directly related to it. Fig. 3, 4, and 8 demonstrates that those changes in $C_{p,cyl}(s/D)$ lead in particular to lower values of C_D, C_m, C_{pb}, $\sqrt{(\overline{C_L'^2})}$, and $\sqrt{(\overline{C_D'^2})}$ at those incidence angles, while the time-averaged global lift coefficient and the Strouhal number remain practically unaffected. In the range of incidence angles from $\alpha = -32°$ to $-45°$ the differences in the mean surface pressures between $Re_D = 2.0 \times 10^5$ and 3.5×10^5 are marginal. That explains the common values for each of the fluid-dynamic coefficients and the Strouhal number at those incidence angles. Hence, at $Re_D = 3.5 \times 10^5$ the flow around the prism slowly migrates from a clear critical Reynolds-number flow state at low absolute incidence angles back to the subcritical one at large absolute incidence angles. The only exception are the somewhat higher values for the fluctuating lift at $Re_D = 3.5 \times 10^5$, which indicates a small increase in the communication between both shear layers in the base region, as well as their interaction with the prism surface.

For $Re_D \geq 5 \times 10^5$, the prism experiences at $\alpha = 0°$ a supercritical Reynolds-number flow, characterised by the presence of a large suction peak of about $C_{p,cyl} = -3.4$ to -3.8 – depending on the exact Reynolds number – at the leading edges of the two lateral faces. Travelling in downstream direction along the two side faces a distinct adverse pressure recovery region, a laminar separation bubble, and a secondary separation of the reattached turbulent boundary layer at the trailing edges of faces *II* and *IV* are encountered (Fig. 6g, 6j, 6m, 6p, and 7). The suction at the base of the prism and the time-averaged global drag are both low, while the symmetric surface pressure distribution induces both a zero time-averaged global lift and mean sectional pitch moment coefficient (Fig. 3). With the exception of $Re_D = 6$ million, both suction peaks (and most probably therefore also both recirculation bubbles) exist until an angle of incidence of about $\alpha = -13°$. At the former Reynolds number, a flat pressure distribution appears on the complete side face *II* as soon as the first non-zero incidence angle has been reached, see Fig. 7.

Interesting to mention is the dynamic behaviour of the heights of the suction peaks and the lengths of the subsequent adverse pressure recovery regions with a variation in Reynolds number. For low

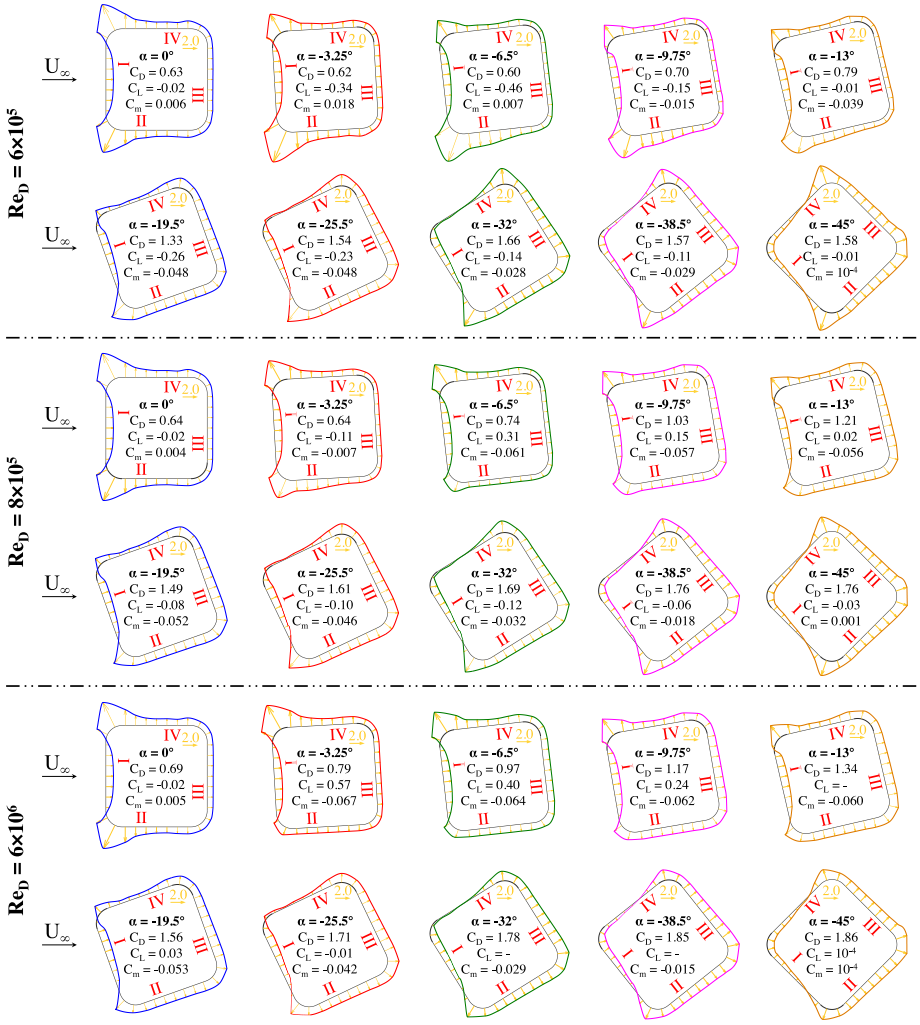

Fig. 7. (*continued*).

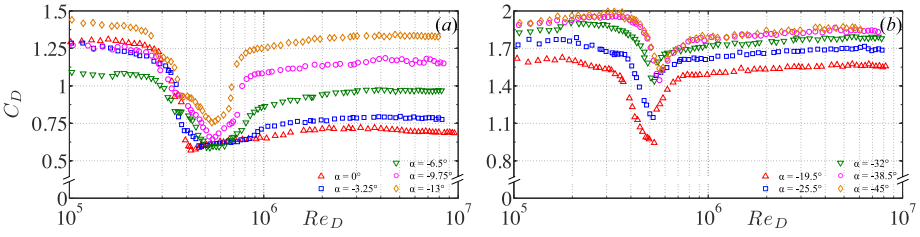

Fig. 8. Time-averaged spanwise-integrated drag coefficient as a function of the Reynolds number for angles of incidence between $\alpha = 0°$ and $-13°$ (left column) and between $\alpha = -19.5°$ and $-45°$ (right column).

Reynolds numbers up to about $Re_D = 4 \times 10^5$–4.5×10^5, an adverse pressure recovery region in combination with a preceding suction peak appears on the upper lateral face only, see, for example, the pressure distributions at $Re_D = 2 \times 10^5$ and 3.5×10^5 in Fig. 7. This explains the occurrence of a positive time-averaged global lift and negative mean sectional pitch moment coefficient for all incidence angles down to $\alpha = -25.5°$ in Fig. 3c to 3f. At Reynolds numbers in the range of $Re_D = 4.5 \times 10^5$ to 6.5×10^5 the lower lateral face experiences a stronger suction peak and a longer adverse pressure recovery region than the upper one, see Fig. 7. This results in a sign inversion of C_L for incidence angles down to $\alpha = -25.5°$ and of C_m down to $\alpha = -9.75°$ to $-13°$. From the surface pressure distributions in Fig. 6m, 6n, and 7 it can be deduced that at $Re_D = 8 \times 10^5$ the situation has changed once more, as the stronger suction peak and the longer adverse pressure recovery region have now both returned to the upper lateral face. From this Reynolds number onwards, the prism experiences once again a steady positive time-averaged global lift and a negative mean sectional pitch moment coefficient at low to moderate absolute incidence angles.

4.2. Susceptibility to transverse galloping and 1-DoF flutter

Consider a visco-elastically supported rigid square-section prism with rounded longitudinal edges that is subjected to a cross-flow and allowed to oscillate with a small amplitude in heave motion only, i.e. being constrained in both its in-line oscillation with the flow and its rotation round the longitudinal axis. By solving the linearised equation of motion in transverse direction, it can be shown that this prism is stable with respect to small-amplitude transverse disturbances around

an equilibrium position when the reduced velocity $U_\infty^\star$ is below a certain threshold (Blevins, 2006):

$$U_\infty^\star = \frac{U_\infty}{f_y D} < \frac{2}{(dC_y/d\alpha)\Big|_{\alpha=\hat{\alpha}}} \frac{4m\pi\zeta_y}{\rho D^2} \tag{3}$$

In this equation, m is the mass per unit length of the rounded square-section prism, ζ_y the structural damping factor, and the term $(dC_y/d\alpha)|_{\alpha=\hat{\alpha}}$ the derivative of the transverse force coefficient C_y (positive upwards) with respect to the angle of incidence at the considered equilibrium angle $\hat{\alpha}$. Based on the linearised quasi-steady theory by Glauert (1919) and Den Hartog (1932), the term $(dC_y/d\alpha)|_{\hat{\alpha}}$ can be approximated by

$$\frac{dC_y}{d\alpha}\bigg|_{\hat{\alpha}} = -\left\{ \frac{dC_L}{d\alpha}\bigg|_{\hat{\alpha}} + C_D(\hat{\alpha}) \right\} \tag{4}$$

where C_L and C_D are the global lift and drag coefficient measured on a static prism, respectively. For those cases at which the aerodynamic damping exceeds the structural one (i.e. a negative net damping), Eq. (3) states that the linear stability threshold for 1-DoF transverse galloping at $\alpha = \hat{\alpha}$ is traversed when (*1*) the term $(dC_L/d\alpha)|_{\hat{\alpha}} + C_D(\hat{\alpha})$ in Eq. (4) is negative (hence, the Glauert/Den Hartog stability criterion) and (*2*) the reduced velocity (Eq. (3)) exceeds its critical value. Under those circumstances, a cross-over from a stable to an unstable oscillatory transverse motion around the equilibrium angle of incidence takes place. By introducing the Scruton number as the reduced damping, i.e. $Sc_y = [2m(2\pi\zeta_y)]/[\rho D^2]$, the critical reduced velocity at which this cross-over occurs can be expressed in a compact form as

$$U_{\infty,cr}^\star = -\frac{2Sc_y}{(dC_L/d\alpha)|_{\hat{\alpha}} + C_D(\hat{\alpha})} \tag{5}$$

In the discussion of the results for C_L as function of the angle of incidence and Reynolds number (Fig. 3c and 3d) it was highlighted that, depending on the actual combination of both parameters, the slope of each $C_L(\alpha)$ curve changes more than once in absolute value and in sign. Together with the values of the global drag coefficient (Fig. 8) these data can be used to analyse the transverse galloping stability of the current rounded square-section prism according to Eq. (5) and localise the Reynolds-number range(s) in which this galloping variant may occur. Fig. 9e shows the resultant stability diagram in terms of $U_{\infty,cr}^\star/Sc_y$ for Reynolds numbers in the range of $Re_D = 1\times10^5$–6×10^6 at four different equilibrium angles between $\hat{\alpha} = 0°$ and $-9.75°$. From this graph it can be inferred that at $\hat{\alpha} = 0°$ two galloping stability boundaries exist in the studied range of Reynolds numbers, namely at $Re_D = 4.63\times10^5$ and 7.92×10^5. According to the classical transverse galloping model, the instability prone-region of the prism is confined to Reynolds numbers that are enclosed by both bounding values. Hence, the prism thus behaves as a soft oscillator only for those Reynolds numbers that belong to the first part of the supercritical Reynolds-number flow regime. A gradual increase in the absolute value of $\hat{\alpha}$ towards $|\hat{\alpha}| = 9.75°$ induces a significant rearrangement of the region(s) in which the prism is susceptible to 1-DoF transverse galloping: bounding Reynolds numbers shift to lower or higher values, new regions of instability appear, while others disappear. At $\hat{\alpha} = -3.25°$, for example, two new galloping-unstable regions can be observed. The first one is limited to a very small range of Reynolds numbers between $Re_D = 3.59\times10^5$ and 3.83×10^5 (hence, within the critical Reynolds-number flow regime). The second one, however, is situated at transcritical Reynolds numbers, bounded to the left at $Re_D = 1.146\times10^6$, while open to the right up to at least $Re_D = 6\times10^6$. Even more interesting is that at both $\hat{\alpha} = -6.5°$ and $-9.75°$ a tendency of the current prism to transverse galloping can be observed for nearly all investigated Reynolds numbers. The only exception is a relatively narrow stability interval covered by Reynolds numbers that belong to the high critical up to low upper transition flow regimes, as well as a second interval for $\hat{\alpha} = -9.75°$ positioned at the transition from the subcritical to the critical flow regime. In addition, the combined reduction of the negative slope of the $C_L(\alpha)$ curves (Fig. 3c and 3d) and the strong increase in C_D (Fig. 8) causes the overall rise of the onset galloping velocity when changing the value of $\hat{\alpha}$ from $-6.5°$ to $-9.75°$.

In contrast to the current results, Carassale et al. (2013) found a clear critical galloping velocity $U_{cr}^\star/Sc$ for all angles of incidence below $\hat{\alpha} = \alpha_{cr}$ in their experiments on a smooth 2D square-section prism with rounded lateral edges of $r/D = 2/15$, placed in a smooth cross-flow at a subcritical Reynolds number of 2.7×10^4. van Hinsberg (2021a) demonstrated that for the current prism configuration with $r/D = 0.16$ at $\alpha = 0°$ an increase in surface roughness has only a marginal effect on the aerodynamics in the subcritical flow regime. Moreover, the presented data clearly showed a strong independence of the mean and fluctuating aerodynamic coefficients from a variation in Reynolds number within that flow regime. It can therefore be argued that the observed difference in transverse galloping stability between the two rounded square-section prisms is mainly caused by the difference in edge roundness of about 20%. This results in a different behaviour of the flow around both prisms (van Hinsberg et al., 2017), with the current prism behaving both aerodynamically and aeroelastically closer to a circular cylinder (being unsusceptible to transverse galloping), while the flow over the prism studied by Carassale et al. is somewhat closer to that around a sharp-edged square-section prism which tends to gallop at all angles of incidence up to $\hat{\alpha} = \alpha_{cr}$. This explains why a clear stability boundary is found for the latter rounded square-section prism up to α_{cr} at the subcritical Reynolds number of $Re_D = 2.7\times10^4$, while the current prism is stable in transverse galloping below $|\alpha| = 6.5°$, as presented in Fig. 9e.

In the case of pure torsional galloping, also known as 1-DoF flutter, the prism performs an LCO in its first torsional mode round its elastic axis (Simiu and Scanlan, 1996; Blevins, 2006). Just like 1-DoF transverse galloping, it occurs when the net damping is negative, hence, the free stream velocity exceeds a certain lower critical threshold, and perturbations in the oncoming flow induce small initial rotational oscillations of the prism round its equilibrium incidence angle. In contrast to the previous galloping variant, the resultant motion of the prism is a rotation round its longitudinal axis in pure pitch, provided that (*1*) the elastic axis of the prism coincides with the axis that goes through the prism's centre of mass and (*2*) its oscillation in-line as well as perpendicular to the oncoming flow are both inhibited. On the basis of a linear quasi-steady analysis, the following critical reduced velocity must be exceeded for pure torsional galloping to occur (Blevins, 2006)

$$U_{\infty,cr}^\star = \frac{U_{\infty,cr}}{f_\theta D} = -\frac{4}{R\,(dC_m/d\alpha)|_{\hat{\alpha}}} \frac{J_\theta 2\pi\zeta_\theta}{\rho D^3} \tag{6}$$

where $(dC_m/d\alpha)|_{\alpha=\hat{\alpha}}$ is the slope of the curve of the static pitch moment coefficient C_m (positive upwards) as function of the incidence angle at $\hat{\alpha}$, J_θ the polar mass moment of inertia round the prism's longitudinal axis per unit length including added-mass effects, and ζ_θ the rotational structural damping factor. Furthermore, R equals the "characteristic radius" associated with a reference point on the cross section of the model at which the relative angle of incidence resulting from the pitch velocity of the prism is calculated. For pure torsion around the central longitudinal axis of the present rounded square-section prism, $R = 0.5D$ could for example be chosen, analogous to the measurements by Nakamura and Mizota (1975) on both sharp-edged square-section prisms and rectangles with various length-to-height ratios which performed harmonic torsional oscillations in a steady cross-flow. By using the torsional Scruton number, $Sc_\theta = [2J_\theta(2\pi\zeta_\theta)]/[\rho D^3 R]$, the critical reduced velocity at $\alpha = \hat{\alpha}$ reads

$$U_{\infty,cr}^\star = -\frac{2Sc_\theta}{(dC_m/d\alpha)|_{\hat{\alpha}}} \tag{7}$$

Eq. (7) shows that the linear stability thresholds for pure torsional galloping are traversed at those points at which a sign reversal of the slope of the $C_m(\alpha)$ curve at $\alpha = \hat{\alpha}$ takes place. Using the sectional aerodynamic moment coefficients of the static prism, reported in Fig. 3e and 3f, the derived instability regions in which torsional galloping

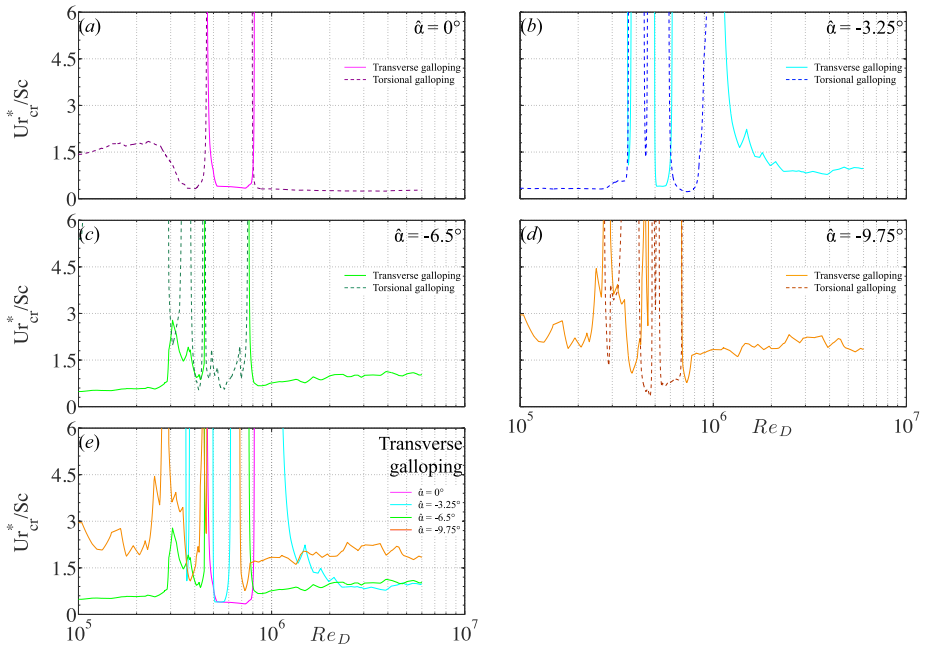

Fig. 9. Stability diagrams for 1-DoF transverse and pure torsional galloping as function of the Reynolds number for four different angles of incidence. (*a*): $\hat{\alpha} = 0°$; (*b*): $\hat{\alpha} = -3.25°$; (*c*): $\hat{\alpha} = -6.5°$; (*d*): $\hat{\alpha} = -9.75°$; (*e*): 1-DoF transverse galloping for $\hat{\alpha} = 0°$ to $-9.75°$. Note that for comparison reasons the values for $U^{\star}_{\infty,cr}/Sc_{\theta}$ have been divided by 6.

becomes possible are presented in Fig. 9a to 9d in terms of $U^{\star}_{\infty,cr}/Sc_{\theta}$ for $1 \times 10^5 \leq Re_D \leq 6 \times 10^6$ at $\hat{\alpha} = 0°$ to $-9.75°$. For comparison reasons, the stability diagrams for 1-DoF transverse galloping at equal value of $\hat{\alpha}$ have also been included in each graph and the values for $U^{\star}_{\infty,cr}/Sc_{\theta}$ have been divided by 6. Surprisingly, with only a few minor exceptions at the non-zero values of $\hat{\alpha}$, the instability regions for torsional galloping (i.e. for $(dC_m/d\alpha)|_{\alpha=\hat{\alpha}} < 0$) appear at those Reynolds numbers at which the Glauert/Den Hartog criterion (Eq. (4)) is not fulfilled and the prism is thus stable in 1-DoF transverse galloping. For $\hat{\alpha} = 0°$ (Fig. 9a) two unstable "soft torsional galloping" regions appear that are bounded at one side only (i.e. at $Re_D = 4.63 \times 10^5$ and 7.92×10^5) and separated by a small stable interval, the latter covered by Reynolds number that belong to the first part of the supercritical flow regime. Based on the present wind tunnel data, a gradual increase in negative value of $\hat{\alpha}$ towards $-9.75°$ results in a progressive reduction of the Reynolds-number ranges in which torsional galloping is predicted to occur. This shrinkage results from the subsequent appearance of an upper stability boundary at $Re_D = 9.24 \times 10^5$ in Fig. 9b, marking the cross-over from the upper transition to the transcritical flow regime at $\hat{\alpha} = -3.25°$, and a lower one at $Re_D = 2.91 \times 10^5$ for $\hat{\alpha} = -6.5°$ at the end of the subcritical flow regime (Fig. 9c).

Although the necessary condition for pure torsional galloping is not met in the stable Reynolds-number ranges, torsional divergence could theoretically take place instead (e.g. Richardson et al. (1965)). For this latter static aeroelastic problem to occur, the sum of the structural stiffness and the aerodynamic torsional stiffness has to approach zero or become negative, which implies that $(dC_m/d\alpha)|_{\hat{\alpha}} \geq 0$. Since at those Reynolds numbers either 1-DoF transverse galloping or torsional divergence could occur, the onset velocity of either one of these two instabilities that is exceeded first will determine which one of the two aeroelastic phenomena will take place. Because the values of the slope of the mean sectional pitch moment coefficient are only slightly positive, e.g. $(dC_m/d\alpha)|_{\hat{\alpha}=0°} = 0$–$0.32$, while the negative values of $(dC_L/d\alpha)|_{\hat{\alpha}}$ are approximately one order of magnitude larger at equal Reynolds number, the aerodynamic damping that counteracts the structural damping is larger in the latter case. It is therefore to be expected that the critical velocity of the 1-DoF transverse galloping instability is exceeded first, although the values of the structural properties of the current prism like the mass moment of inertia, the weight, the natural frequency, and the structural damping ratios in transverse and torsional direction play an important role as well (Blevins, 2006; Païdoussis et al., 2011).

The results presented in this section clearly show that 1-DoF transverse galloping and pure torsional galloping can still take place under certain conditions, even though the respective classical galloping model predicts a stable situation. For this to happen, not only the critical reduced velocity has to be exceeded, but, in contrast to the soft oscillator variant at $\hat{\alpha} = 0°$, the prism also has to be given a certain minimum initial transverse or rotational amplitude in order to be set in an unstable galloping condition. At those Reynolds numbers, the prism thus behaves as a hard oscillator.

5. Conclusions

Experimental data on the unsteady and time-averaged aerodynamics of a static 2D square-section prism with rounded lateral edges of $r/D = 0.16$ and fully covered by a light surface roughness of $k_s/D = 4.5 \times 10^{-4}$ have been obtained through tests in the High-Pressure Wind Tunnel of the DLR in Göttingen. Their analysis has revealed that both the separate and combined variation in the Reynolds number in the range of $Re_D = 1 \times 10^5$–8×10^6 – hence, covering all Reynolds-number flow regimes from subcritical up to high transcritical – and in the angle of incidence between $\alpha = -45°$ and $+3.25°$ have a drastic effect on the surface pressure distribution along the cross-section at the mid-span of the prism. It has been proven that the prism's cross-sectional edge roundness plays a key role in the behaviour of the flow and thus in the values of the surface pressures, resultant aerodynamic forces, pitch moment, and shedding process of the eddies in the wake of the prism. By applying the linearised quasi-steady aerodynamic modelling to those data, the proneness of the prism to both 1-DoF transverse and torsional galloping (i.e. 1-DoF flutter) and their instability regions in terms of the Reynolds number and incidence angle have been investigated. The main results can be summarised as follows:

1. Positioned at $\alpha = 0°$, the prism experiences a supercritical flow at least up to a Reynolds number of 10 million. At the first investigated non-zero angle of incidence, i.e. $|\alpha| = 3.25°$, the upper limit of this Reynolds-number flow regime becomes visible in the studied range of Reynolds numbers. The upper boundary gradually shifts to lower Reynolds numbers with increasing absolute value of the angle of incidence, thereby reducing the supercritical Reynolds-number flow regime step by step to a single point. As a result, the two uppermost Reynolds-number flow regimes, hence, the upper transition and the transcritical flow regime, appear as well and gradually spread over an increasing range of Reynolds numbers with increasing absolute incidence angle. In contrast, the length of both the subcritical and the critical Reynolds-number flow regime, as well as the two bounding Reynolds numbers of the latter flow regime, remain nearly unaffected by a change in α. Either a gradual recovery of the aerodynamic coefficients and Strouhal number occurs for all non-zero angles of incidence in the upper transition or a sudden discontinuous step from the supercritical Reynolds-number flow state into the transcritical one takes place. The transcritical values of those parameters are therefore at a similar level as in the subcritical Reynolds-number flow regime for the majority of the angles of incidence.
2. For specific combinations of the two governing parameters a complete suppression of the periodic eddy shedding is possible. This is the case in a limited range of Reynolds numbers that belongs to the upper transition and only for incidence angles in the range of $|\alpha| = 3.25°$–$19.5°$. This particular behaviour at Reynolds numbers in the upper transition is actually already known from experimental studies on 2D smooth circular cylinders, but has until now never been demonstrated for rounded square-section prisms.
3. The critical angle of incidence, α_{cr}, at which the detached flow reattaches on the prism's side face that is turned into the oncoming free stream, lies close to $\alpha = -6.5°$. In comparison to 2D smooth square-section prisms with sharp edges (i.e. $r/D = 0$) for which the critical angle of incidence is positioned at $\alpha = 12°$–$15°$, the currently applied edge roundness thus produces a reduction of α_{cr} by roughly 50%–60%. The effect on the flow over the current prism in the vicinity of the critical angle of incidence becomes clearly visible by the presence of a singular point in the curves of the aerodynamic coefficients as function of the incidence angle. While for all aerodynamic coefficients an inversion of the slope of their curves emerges at this angle of incidence, the $St_L(\alpha)$ curves either show such an inversion as well or possess a strong discontinuity with a step from a high Strouhal-number value down to a much lower one.
4. The crossover from the critical into the supercritical Reynolds-number flow regime is characterised by an opposite sign switch of both the time-averaged global lift and mean sectional pitch moment slopes for $\alpha = 0°$ at $Re_D = 4.5 \times 10^5$–4.6×10^5, the former from positive to negative and the latter from negative to positive values. A second sign inversion of $dC_L/d\alpha|_{\alpha=0°}$ and $dC_m/d\alpha|_{\alpha=0°}$ appears at the transition between the supercritical Reynolds-number flow regime and the upper transition, hence, at $Re_D = 7.9 \times 10^5$–8.2×10^5. This sign switching is in both cases induced by the relocation of the stronger suction peak and the ensuing longer separation bubble (visible by the adverse pressure recovery region) from one upstream lateral rounded edge and side face to the ones at the opposite side of the prism.
5. On the basis of the outcomes of the classical 1-DoF transverse and rotational galloping models, the prism can be characterised both as a soft and a hard oscillator, depending on the value of the Reynolds number. At an equilibrium incidence angle of $\hat{\alpha} = 0°$ (hence, the soft oscillator case), the instability region in which transverse galloping becomes possible is limited to a small range of Reynolds numbers within the supercritical flow regime. For all other Reynolds numbers, the current prism is potentially unstable to 1-DoF rotational galloping. An increase in the equilibrium angle of incidence induces significant shifts of the galloping onset velocities. While for larger initial excitations of the prism the potentially unstable regions of transverse galloping gradually spread over larger ranges of Reynolds numbers and even become unbounded at their lower or upper side, the exact opposite occurs for rotational galloping. For the latter, a gradual increase in $\hat{\alpha}$ leads to a progressive reduction of the instability regions, first at transcritical Reynolds numbers for $\hat{\alpha} = -3.25°$, then also at subcritical ones for $\hat{\alpha} = -6.5°$, which results from the subsequent appearance of an absolute upper and lower stability boundary.

The rounded lateral edges of the square-section prism allow a wandering of the primary and secondary flow separation points back and forth over the those curved edges. The resultant changes in the spread of the free shear layers upon separation from the windward-directed edges lead to variations in the reattachment locations of the free shear layers on both side faces with variations in both the Reynolds number and the incidence angle. This results in a distinct fluctuations in the sectional surface pressure distribution and thus in the time-dependent aerodynamics of the prism. Ultimately, it is those changes in C_D, C_L and C_m with incidence angle and Reynolds number that are responsible for the possible appearance of 1-DoF transverse and pure torsional galloping in certain Reynolds-number flow regimes. Whether one of these aeroelastic instabilities does indeed occur at a certain Reynolds number depends, among other factors, on the value of the Scruton number.

CRediT authorship contribution statement

Nils Paul van Hinsberg: Writing – review & editing, Writing – original draft, Visualization, Validation, Supervision, Software, Resources, Project administration, Methodology, Investigation, Formal analysis, Data curation, Conceptualization. **Annika Frede:** Writing – review & editing, Writing – original draft, Visualization, Validation, Supervision, Software, Resources, Project administration, Methodology, Investigation, Formal analysis, Data curation, Conceptualization.

Declaration of competing interest

The authors declare that they have no known competing financial interests or personal relationships that could have appeared to influence the work reported in this paper.

Acknowledgements

Technical assistance of Markus Löhr of the DLR Institute of Aeroelasticity and Karsten Steiner of DNW is gratefully acknowledged. DLR Systemhaus Technik and Deharde are recognised for the construction and manufacturing of the wind tunnel model, respectively.

Funding

This research did not receive any specific grant from funding agencies in the public, commercial, or not-for-profit sectors.

Data availability

Data will be made available on request.

References

Achenbach, E., Heinecke, E., 1981. On vortex shedding from smooth and rough cylinders in the range of Reynolds numbers 6×10^3 to 5×10^6. J. Fluid Mech. 109 (109), 239–251. http://dx.doi.org/10.1017/S002211208100102X.

Adams, T., Grant, C., Watson, H., 2012. A simple algorithm to relate measured surface roughness to equivalent sand-grain roughness. Int. J. Mech. Eng. Mechatron. 1, 66–71. http://dx.doi.org/10.11159/ijmem.2012.008.

Alam, M.M., Abdelhamid, T., Sohankar, A., 2020. Effect of cylinder corner radius and attack angle on heat transfer and flow topology. Int. J. Mech. Sci. 175, 105566–1–14. http://dx.doi.org/10.1016/j.ijmecsci.2020.105566.

Allen, H.J., Vincenti, W.G., 1944. Wall interference in a two-dimensional flow wind tunnel with consideration of the effect of compressibility. Technical report 782, Nat. Adv. Comm. Aero. Report, http://dx.doi.org/10.1017/S002211206600020X.

Bai, H., Alam, M.M., 2018. Dependence of square cylinder wake on Reynolds number. Phys. Fluids 30, 015102–1–19. http://dx.doi.org/10.1063/1.4996945.

Bearman, P.W., 1972. An investigation of the flow around rectangular cylinders. Aeronaut. Q. 23, 229–237. http://dx.doi.org/10.1017/S0001925900006119.

Blevins, R.D., 2006. Flow-Induced Vibration. Second Edition Reprint. Krieger Publishing Company, Malabar, Florida, USA.

Carassale, L., Freda, A., Marré-Brunenghi, M., 2013. Effects of free-stream turbulence and corner shape on the galloping instability of square cylinders. J. Wind Eng. Ind. Aerodyn. 123, 274–280. http://dx.doi.org/10.1016/j.jweia.2013.09.002.

Carassale, L., Freda, A., Marré-Brunenghi, M., 2014. Experimental investigation on the aerodynamic behavior of square cylinders with rounded corners. J. Fluid Struct. 44, 195–204. http://dx.doi.org/10.1016/j.jfluidstructs.2013.10.010.

Chen, J.M., Liu, C.-H., 1999. Vortex shedding and surface pressures on a square cylinder at incidence to a uniform air stream. Int. J. Heat Fluid Fl. 20, 592–597. http://dx.doi.org/10.1016/S0142-727X(99)00047-8.

Delany, N.K., Sorensen, N.E., 1953. Low speed drag of cylinders of various shapes. Technical Report 3038, Nat. Adv. Comm. Aero. Technical Note.

Den Hartog, J.P., 1932. Transmission line vibration due to sleet. Trans. Am. Inst. Electr. Eng. 51 (4), 1074–1076. http://dx.doi.org/10.1109/T-AIEE.1932.5056223.

Dutta, S., Muralidhar, K., Panigrahi, P.K., 2003. Influence of the orientation of a square cylinder on the wake properties. Exp. Fluids 34, 16–23. http://dx.doi.org/10.1007/s00348-002-0484-x.

Fage, A., Warsap, J.H., 1929. The effect of turbulence and surface roughness on the drag of a circular cylinder. Technical Report 3038, Aeron. Res. Comm. Tech. Reports & Memoranda.

Fitridge, I., Dempster, T., Guenther, J., de Nys, R., 2012. The impact and control of biofouling in marine aquaculture: a review. Biofouling 28 (7), 649–669. http://dx.doi.org/10.1080/08927014.2012.700478.

Forteath, G.N.R., Picken, G.B., Ralph, R., Williams, J., 1982. Marine Growth Studies on the North Sea Oil Platform Montrose Alpha. Mar. Ecol. Prog. Ser. 8, 61–68. http://dx.doi.org/10.3354/meps008061.

Glauert, H., 1919. The rotation of an aerofoil about a fixed axis. Technical Report 595, Advisory Committee for Aeronautics.

Gupta, S., Wipf, T.J., Fanous, F., Baenziger, M., Hahm, Y.H., 1994. Structural failure analysis of 345 kV transmission line. IEEE Trans. Power Deliv. 9 (2), 894–903. http://dx.doi.org/10.1109/61.296272.

Huang, R.F., Lin, B.H., 2011. Effects of flow patterns on aerodynamic forces of a square cylinder at incidence. J. Mech. 03, 347–355. http://dx.doi.org/10.1017/jmech.2011.37.

Huang, R.F., Lin, B.H., Yen, S.C., 2010. Time-averaged topological flow patterns and their influence on vortex shedding of a square cylinder in crossflow at incidence. J. Fluid Struct. 26, 406–429. http://dx.doi.org/10.1016/j.jfluidstructs.2010.01.003.

Igarashi, T., 1984. Characteristics of the flow around a square prism. Bull. JSME 27 (231), 1858–1865. http://dx.doi.org/10.1299/jsme1958.27.1858.

Kerckhof, F., Rumes, B., Jacques, T., Degraer, S., Norro, A., 2010. Early development of the subtidal marine biofouling on a concrete offshore windmill foundation on the Thornton Bank (southern North Sea): first monitoring results. I. J. Soc. for Underw. Technol. 29 (3), 137–149. http://dx.doi.org/10.3723/ut.29.137.

Knisely, C.W., 1990. Strouhal numbers of rectangular cylinders at incidence, A review and new data. J. Fluid Struct. 4, 371–393. http://dx.doi.org/10.1016/0889-9746(90)90137-T.

Langhamer, O., Wilhelmsson, D., Engström, J., 2009. Artificial reef effect and fouling impacts on offshore wave power foundations and buoys - a pilot study. Estuar., Coast. and Shelf Sci. 82, 426–432. http://dx.doi.org/10.1016/j.ecss.2009.02.009.

Lee, B.E., 1975. The effect of turbulence on the surface pressure field of a square prism. J. Fluid Mech. 69, 321–352. http://dx.doi.org/10.1017/S0022112075001437.

Luo, S.C., Chew, Y.T., Ng, Y.T., 2003. Characteristics of square cylinder wake transition flows. Phys. Fluids 15 (9), 2549–2559. http://dx.doi.org/10.1063/1.1596413.

Luo, S.C., Yazdani, M.G., Chew, Y.T., Lee, T.S., 1994. Effects of incidence and afterbody shape on flow past bluff cylinders. J. Wind. Eng. Ind. Aerodyn. 53, 375–399. http://dx.doi.org/10.1016/0167-6105(94)90092-2.

Lyn, D.A., Einav, S., Rodi, W., Park, J.-H., 1995. A Laser-Doppler velocimetry study of ensemble-averaged characteristics of the turbulent near wake of a square cylinder. J. Fluid Mech. 304, 285–319. http://dx.doi.org/10.1017/S0022112095004435.

Moe, G., Henriksen, M.O., 1999. Flow induced vibrations of line-like structures. In: Proc. 3rd Int. Symp. Cable Dyn..

Nakamura, Y., 1979. On the aerodynamic mechanism of torsional flutter of bluff structures. J. Sound Vib. 67 (2), 163–177. http://dx.doi.org/10.1016/0022-460X(79)90481-4.

Nakamura, Y., Hirata, K., 1989. Critical geometry of oscillating bluff bodies. J. Fluid Mech. 208, 375–393. http://dx.doi.org/10.1017/S0022112089002879.

Nakamura, Y., Hirata, K., 1991. Pressure fluctuations on oscillating rectangular cylinders with the long side normal to the flow. J. Fluid Struct. 5, 165–183. http://dx.doi.org/10.1016/0889-9746(91)90460-7.

Nakamura, Y., Hirata, K., 1994. The aerodynamic mechanism of galloping. Trans. Jpn Soc. Aerospace Sci. 36, 257–269.

Nakamura, Y., Matsukawa, T., 1987. Vortex excitation of rectangular cylinders with a long side normal to the flow. J. Fluid Mech. 180, 171–191. http://dx.doi.org/10.1017/S0022112087001770.

Nakamura, Y., Mizota, T., 1975. Torsional flutter of rectangular prisms. ASCE J. Eng. Mech. Div. 101 (2), 125–142. http://dx.doi.org/10.1061/JMCEA3.0002001.

Naudascher, E., Rockwell, D., 1994. Flow-Induced Vibrations: An Engineering Guide. Dover Publications, Inc., Mineola, USA.

Norberg, C., 1993. Flow around rectangular cylinders: pressure forces and wake frequencies. J. Wind. Eng. Ind. Aerodyn. 49, 187–196. http://dx.doi.org/10.1016/0167-6105(93)90014-F.

Obasaju, E.D., 1983. An investigation of the effects of incidence on the flow around a square section cylinder. Aeronaut. Q. 34 (4), 243–259. http://dx.doi.org/10.1017/S0001925900009768.

Okajima, A., 1982. Strouhal numbers of rectangular cylinders. J. Fluid Mech. 123, 379–398. http://dx.doi.org/10.1017/S0022112082003115.

Païdoussis, M.P., Price, S.J., de Langre, E., 2011. Fluid-Structure Interactions. Cross-Flow-Induced Instabilities. Cambridge University Press, Cambridge, UK.

Parkinson, G.V., 1989. Phenomena and modelling of flow-induced vibrations of bluff cylinders. Prog. Aerosp. Sci. 26 (2), 169–224. http://dx.doi.org/10.1016/0376-0421(89)90008-0.

Polhamus, E.C., 1958. Effect of flow incidence and Reynolds number on low-speed aerodynamic characteristics of several noncircular cylinders with applications to directional stability and spinning. Technical Report 4176, Nat. Adv. Comm. Aero. Technical Note.

Richardson, S.A.J., Martucelli, J.R., Price, W.S., 1965. Research study on galloping of electric power transmission lines. Part 1. In: Proc. 1st Int. Conf. Wind Effects on Buildings and Structures. pp. 612–686.

Rockwell, D.O., 1977. Organized fluctuations due to flow past a square cross section cylinder. J. Fluids Eng. 99 (3), 511–516. http://dx.doi.org/10.1115/1.3448831.

Roshko, A., 1961. Experiments on the flow past a circular cylinder at very high Reynolds number. J. Fluid Mech. 10, 345–356. http://dx.doi.org/10.1017/S0022112061000950.

Simiu, E., Scanlan, R.H., 1996. Wind Effects on Structures: Fundamentals and applications to design. John Wiley, New York, USA.

Slater, J.E., 1969. Aeroelastic Instability of a Structural Angle Section (Ph.D. thesis). University of British Columbia, Vancouver, Canada.

Sohankar, A., Mohagheghian, S., Dehghan, A.A., Dehghan Manshadi, M., 2015. A smoke visualization study of the flow over a square cylinder at incidence and tandem square cylinders. J. Vis. 18, 687–703. http://dx.doi.org/10.1007/s12650-015-0275-0.

Tamura, T., Miyagi, T., 1999. The effect of turbulence on aerodynamic forces on a square cylinder with various corner shapes. J. Wind. Eng. Ind. Aerodyn. 83, 135–145. http://dx.doi.org/10.1016/S0167-6105(99)00067-7.

Tamura, T., Miyagi, T., Kitagishi, T., 1998. Numerical prediction of unsteady pressures on a square cylinder with various corner shapes. J. Wind. Eng. Ind. Aerodyn. 74–76, 531–542. http://dx.doi.org/10.1016/S0167-6105(98)00048-8.

Theophanatos, A., 1988. Marine Growth and the Hydrodynamic Loading of Offshore Structures (Ph.D. thesis). Strathclyde University, Glasgow, United Kingdom, http://dx.doi.org/10.48730/qx63-8r70.

Valentín, D., Valero, C., Egusquiza, M., Presas, A., 2022. Failure investigation of a solar tracker due to wind-induced torsional galloping. Eng. Fail. Anal. 135, http://dx.doi.org/10.1016/j.engfailanal.2022.106137, 106137–1–11.

van Hinsberg, N.P., 2021a. Mean and unsteady loading on square prisms with rounded edges: hard marine growth, incidence, and Reynolds number effects. Mar. Struct. http://dx.doi.org/10.1016/j.marstruc.2020.102886.

van Hinsberg, N.P., 2021b. Aerodynamics of smooth and rough square-section prisms at incidence in very high Reynolds-number cross-flows. Exp. Fluids 62 (50), 1–17. http://dx.doi.org/10.1007/s00348-021-03143-5.

van Hinsberg, N.P., Schewe, G., Jacobs, M., 2017. Experiments on the aerodynamic behaviour of square cylinders with rounded corners at Reynolds numbers up to 12 million. J. Fluid Struct. 74, 214–233. http://dx.doi.org/10.1016/j.jfluidstructs.2017.08.002.

van Hinsberg, N.P., Schewe, G., Jacobs, M., 2018. Experimental investigation on the combined effects of surface roughness and corner radius for square cylinders at high Reynolds numbers up to 10^7. J. Wind. Eng. Ind. Aerodyn. 173, 14–27. http://dx.doi.org/10.1016/j.jweia.2017.12.003.

van Oudheusden, B.W., Scarano, F., van Hinsberg, N.P., Roosenboom, E.W.M., 2007. Quantitative visualization of the flow around a square-section cylinder at incidence. J. Wind. Eng. Ind. Aerodyn. 96, 1–10. http://dx.doi.org/10.1016/j.jweia.2007.06.030.

van Oudheusden, B.W., Scarano, F., van Hinsberg, N.P., Watt, D.W., 2005. Phase-resolved characterization of vortex shedding in the near wake of a square-section cylinder at incidence. Exp. Fluids 39, 86–98. http://dx.doi.org/10.1007/s00348-005-0985-5.

Vickery, B.J., 1966. Fluctuating lift and drag on a long cylinder of square cross-section in a smooth and a turbulent stream. J. Fluid Mech. 25, 481–494. http://dx.doi.org/10.1017/S002211206600020X.

Yen, S.C., Yang, C.W., 2011. Flow patterns and vortex shedding behavior behind a square cylinder. J. Wind. Eng. Ind. Aerodyn. 99, 868–878. http://dx.doi.org/10.1016/j.jweia.2011.06.006.